Article

Cell Reports

Drug-repurposing screen on patient-derived organoids identifies therapy-induced vulnerability in KRAS-mutant colon cancer

Graphical abstract

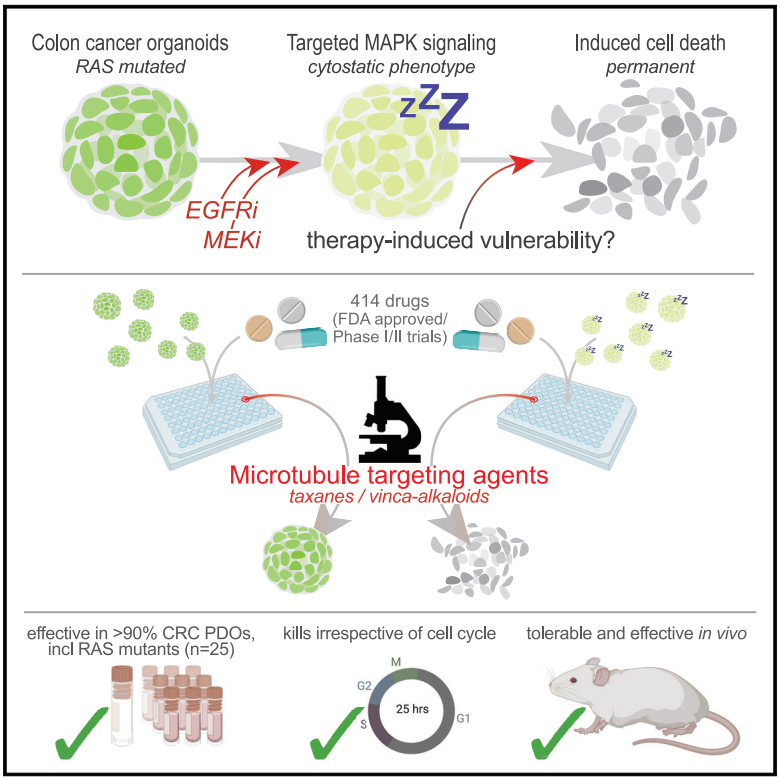

Highlights

- Imaging-based screening on organoids enables scoring of drug-induced cell killing
- Targeting MAPK signaling sensitizes colon cancers for microtubule-targeting agents
- Combining MAPK pathway inhibition and vinorelbine is tolerable and effective *in vivo*
- Induced cell killing by the combination therapy is independent of cell-cycle stage

Authors

Sander Mertens, Maarten A. Huismans, Carla S. Verissimo, ..., Jeanine M.L. Roodhart, Johannes L. Bos, Hugo J.G. Snippert

Correspondence

h.j.g.snippert@umcutrecht.nl

In brief

Targeted therapies against KRAS-mutant colorectal cancers have proven to be problematic, whereby induction of cytotoxicity remains incomplete even upon effective suppression of downstream MAPK pathway activity. Mertens et al. find that effective inhibition of MAPK signaling sensitizes cancer cells for microtubule-targeting agents.

Mertens et al., 2023, Cell Reports *42*, 112324
April 25, 2023
https://doi.org/10.1016/j.celrep.2023.112324

CellPress

Cell Reports

CellPress
OPEN ACCESS

Article

Drug-repurposing screen on patient-derived organoids identifies therapy-induced vulnerability in KRAS-mutant colon cancer

Sander Mertens,[1] Maarten A. Huismans,[1] Carla S. Verissimo,[1,7] Bas Ponsioen,[1] Rene Overmeer,[2] Natalie Proost,[3] Olaf van Tellingen,[3,4] Marieke van de Ven,[3] Harry Begthel,[5] Sylvia F. Boj,[2] Hans Clevers,[5,8] Jeanine M.L. Roodhart,[1,6] Johannes L. Bos,[1] and Hugo J.G. Snippert[1,9,*]

[1]Oncode Institute, Center for Molecular Medicine, University Medical Center Utrecht, Utrecht, the Netherlands
[2]Hubrecht Organoid Technology (HUB), Utrecht, the Netherlands
[3]Mouse Clinic for Cancer and Aging Research (MCCA), Preclinical Intervention Unit, the Netherlands Cancer Institute, 1066 CX Amsterdam, the Netherlands
[4]Division of Clinical Pharmacology, the Netherlands Cancer Institute, 1066 CX Amsterdam, the Netherlands
[5]Oncode Institute, Hubrecht Institute-KNAW, University Medical Center Utrecht, Utrecht, the Netherlands
[6]Department of Medical Oncology, University Medical Center Utrecht, Utrecht, the Netherlands
[7]Present address: Hubrecht Organoid Technology (HUB), Utrecht, the Netherlands
[8]Present address: Pharma, Research and Early Development (pRED) of F. Hoffmann-La Roche Ltd, Basel, Switzerland
[9]Lead contact
*Correspondence: h.j.g.snippert@umcutrecht.nl
https://doi.org/10.1016/j.celrep.2023.112324

SUMMARY

Patient-derived organoids (PDOs) are widely heralded as a drug-screening platform to develop new anti-cancer therapies. Here, we use a drug-repurposing library to screen PDOs of colorectal cancer (CRC) to identify hidden vulnerabilities within therapy-induced phenotypes. Using a microscopy-based screen that accurately scores drug-induced cell killing, we have tested 414 putative anti-cancer drugs for their ability to switch the EGFRi/MEKi-induced cytostatic phenotype toward cytotoxicity. A majority of validated hits (9/37) are microtubule-targeting agents that are commonly used in clinical oncology, such as taxanes and vinca-alkaloids. One of these drugs, vinorelbine, is consistently effective across a panel of >25 different CRC PDOs, independent of RAS mutational status. Unlike vinorelbine alone, its combination with EGFR/MEK inhibition induces apoptosis at all stages of the cell cycle and shows tolerability and effective anti-tumor activity *in vivo*, setting the basis for a clinical trial to treat patients with metastatic RAS-mutant CRC.

INTRODUCTION

The EGFR-RAS-MAPK pathway is among the most frequently deregulated signaling cascades in colorectal cancer (CRC), but effective therapeutic strategies to target KRAS or BRAF-mutant CRC tumors have proven to be problematic.[1,2] Although oncogenic driver mutations prompt the constitutive activation of KRAS[3] and BRAF,[4] the most promising clinical results encompass inhibition of the mitogen-activated protein kinase (MAPK) pathway in combination with the upstream epidermal growth factor receptor (EGFR).[5–8] However, in particular for RAS-mutant CRC, such combinatorial targeting of the EGFR-RAS-MAPK pathway results in disease stabilization at best,[9–11] highlighting that induction of cytotoxicity remains problematic in RAS-mutant tumors with sole suppression of downstream MAPK pathway activity.

Over the past years, genetic screens on 2D cell lines have documented specific vulnerabilities in RAS-mutant cancers.[12,13] However, the success of these approaches in identifying viable therapeutic strategies that target RAS-driven tumor growth has been limited.[1,14] In contrast, effective inhibition of downstream MAPK pathway signaling demonstrated significant anti-tumor activity in mice.[15] Unfortunately, the required doses of targeted inhibitors to be effective against the EGFR-MAPK pathway are invariably accompanied by poor tolerability.[1] Therefore, rather than improving effectivity of EGFR-MAPK pathway inhibition beyond levels that are associated with toxicity, there is high potential in exploring additional targets. One possibility is to convert the cytostatic effect of EGFR-MAPK pathway suppression into cytotoxicity by co-targeting therapy-induced vulnerabilities. Indeed, co-targeting the apoptotic pathway using genetic depletion or pharmacological inhibition of BCL-xL has been reported as a valid strategy.[16,17] However, acute thrombocytopenia is a known dose-limiting toxicity regarding direct BCL-xL inhibition.[18,19]

Patient-derived organoids (PDOs) of CRC are robust *in vitro* models that retain the histopathological features of *in vivo* tumors.[20,21] In particular, their potential to recapitulate patient-specific drug sensitivities fuel their anticipated role in personalized anti-cancer care.[22–25] In addition, their scalability over

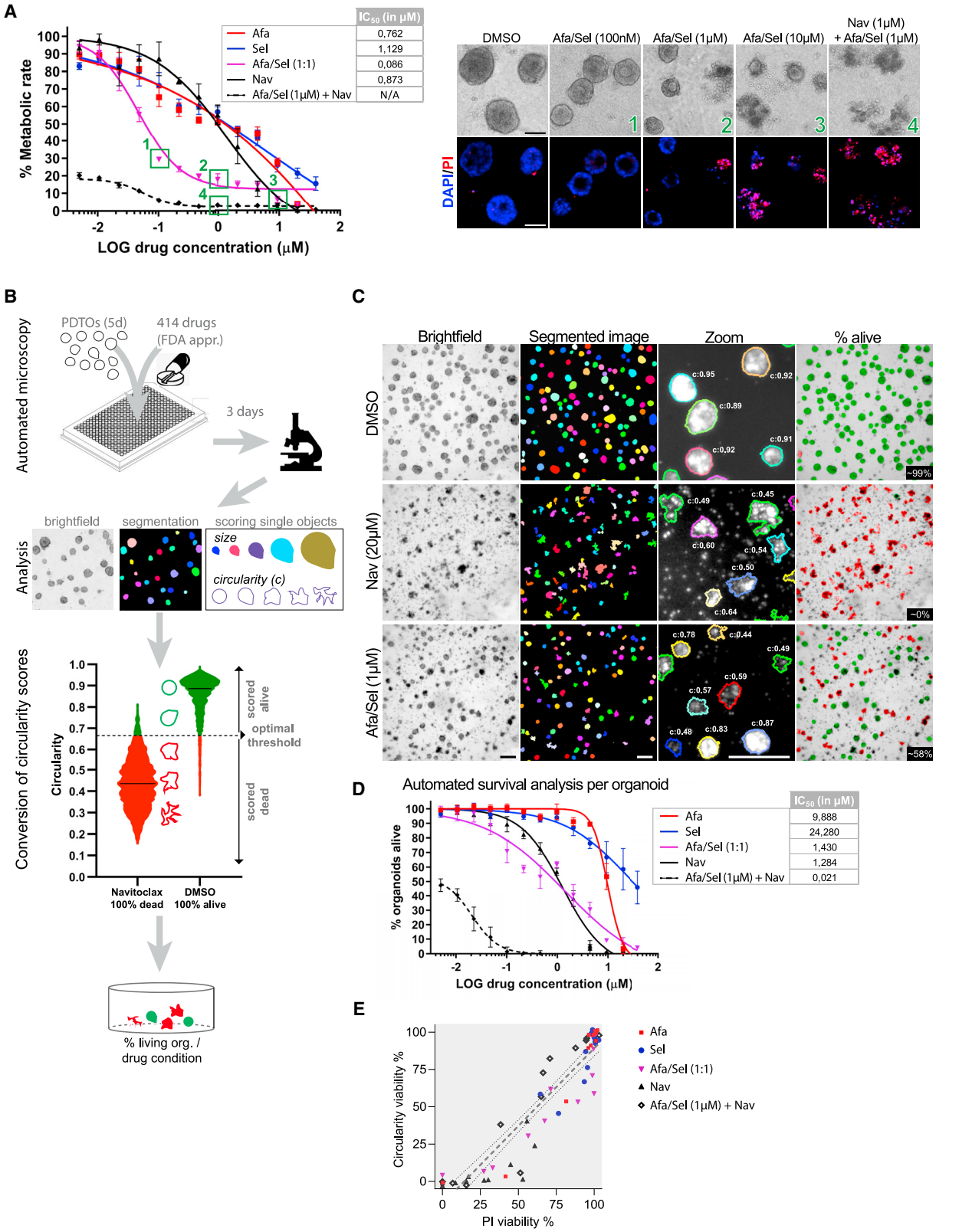

(legend on next page)

patient-derived xenograft (PDX) models is of high interest for the purpose of pre-clinical drug screenings, either for pharmaceutical drug discovery and development or for drug-repurposing strategies through the identification of new effective combinations of approved or investigational drugs.[26] Indeed, drug screens of organoid platforms of CRC are commonly reported, but these are predominantly performed to identify new genotype-phenotype correlations,[17,21,27] to demonstrate the organoid's ability to predict patient-specific drug sensitivity,[22–24,28] or to classify compound induced organoid phenotypes.[29,30] Strikingly, despite the potential that is attributed to pre-clinical drug screens of PDOs to revolutionize drug discovery and therapy development against cancer, dedicated drug screens of tumor PDOs are scarcely reported.[31]

To identify drug candidates that can switch the pan-HERi/MEKi-induced cytostatic phenotype in KRAS-mutant CRCs into cytotoxicity, we established a robust imaging-based screening method for PDOs that discriminates cytostatic from drug-induced cytotoxicity. Screening a repurposing library of >400 Food and Drug Administration (FDA)-approved and experimental compounds, with extensive follow-up of positive hits on >25 CRC PDOs and in various assays including dose toxicity in PDX models, we validated microtubule-targeting agents (MTAs) as a single class of compounds to be most effective when co-administered with EGFR/MEK inhibition. Our findings showcase that pre-clinical drug screens on therapy-challenged PDOs can identify hidden vulnerabilities within the therapy-induced phenotypes that are amenable for clinical follow-up.

RESULTS

High-content screening of drug-induced cytotoxicity in patient-derived tumor organoids

Screening drug candidates for anti-cancer effectivity on human tumor organoids is commonly performed using high-throughput metabolic readouts (reviewed by Wensink et al.[25]). Although informative to score patterns between drug sensitivity and cancer mutations, an important caveat in such assays is the lack of discrimination between cytostatic and cytotoxic drug effects.[17,32] Illustrative is targeted inhibition of the EGFR-RAS-MAPK pathway in KRAS-mutant tumor organoids (CRC PDOs) with a clinically relevant combination of pan-HER and MEK inhibitors. While the drug-induced effects are accompanied by significant reductions in metabolic rates, microscopic analysis shows minor induction of the desired cell death (Figure 1A). The inability to faithfully detect cell death with commonly used high-throughput assays is detrimental to identifying new therapeutic vulnerabilities in KRAS-mutant tumors that enhance anti-cancer effectivity of combined EGFR and MEK inhibition.

Recent advances in automated microscopy and image analysis enable sophisticated strategies to score drug-induced phenotypes in 3D model systems.[29,31–33] To screen for drug-induced cytotoxicity in PDOs, we developed a semi-automated image analysis pipeline centered on wide-field imaging of organoid cultures in 384-well plates (Figure 1B). Fluorescent images of organoid cultures were segmented into single objects (~250 organoids per well) and analyzed for parameters such as circularity and size. In particular, the circularity score (C score: the relation between the square root of organoid area over its circumference, normalized to 1.0 for a perfect circle) served as a reliable readout for drug-induced cytotoxicity, as cell death affects epithelial integrity and reduces circularity of the normally near-cystic morphology. Comparison between all the organoid's C scores within a healthy culture (100% alive) versus 100% drug-induced cytotoxicity (confirmed by propidium iodide [PI] staining, Figure S1A) indeed revealed a minimal overlap between the C-score distributions of these organoid populations (Figure 1B, violin plots).

To convert C scores per organoid into survival scores for an organoid population, we determined a threshold that optimally classifies organoids as alive or dead per screening plate using inherent controls (Figure 1C). Using this method, treatment of KRAS-mutant PDOs with a clinically relevant therapeutic combination of pan-HER inhibitor afatinib (Afa) and MEK inhibitor selumetinib (Sel) was estimated to kill ≈42% of the organoids

Figure 1. High-content screening of drug-induced cytotoxicity in patient-derived tumor organoids

(A) Left: dose-response curves based on a metabolic assay on P9T CRC PDOs treated for 72 h with 13 concentrations of the indicated targeted drugs as monotherapy or combinations thereof. Afatinib (Afa) + selumetinib (Sel) were both fixed at 1 μM when combined with navitoclax (Nav). Curves were generated by non-linear regression fitting upon normalization to control conditions (DMSO) and a toxic dose of Nav. Data are represented as means ± SD (of ≥2 technical replicates). Table summarizes drug IC_{50} values. Numbered green boxes refer to images displayed on the right: representative images of organoids after treatment. Top row, bright-field images; bottom row, DAPI (blue) marks all cells and propidium iodide (PI) marks dead cells. Large discrepancy was observed between actual viability of the organoids and the loss of metabolic activity (e.g., compare box 1 [left] with panel 1 [right] and box 2 with panel 2). Scale bars, 50 μm.

(B) Overview of high-content screening method to score drug-induced cytotoxicity in CRC PDO cultures. Five-day-old PDO P9T cultures were subjected to treatment with a drug-repurposing library of 414 compounds, either as single agents or in combination with Afa/Sel (both fixed at 1 μM). Wide-field images of 72-h-treated cultures were segmented into single objects and analyzed for area (size) and circularity (C). To convert circularity scores into viability scores, a threshold is determined per 384-well plate that provides optimal discrimination between C-score distributions of negative control (DMSO) vs. positive controls (Nav at toxic dose of 20 μM). Subsequently, optimal threshold is applied to score viability of each individual organoid per 384-well plate. Viability of ≥1,900 segmented organoids (from ≥3 technical replicates) was determined per drug condition.

(C) Representative images demonstrating the use of C scores per organoid to define drug-induced cytotoxicity. DMSO (top row) and Nav (20 μM, middle row) were used as negative and positive control, respectively. Applying the optimal threshold per organoid's C score (third column) yields percentage of living organoids (green objects in fourth column) per drug condition. Bottom row shows mixed cytostatic/cytotoxic phenotype of Afa/Sel (1 μM). Scale bars, 200 μm.

(D) Dose-response curves obtained using the high-content screening assay, scoring object circularity as a measure of drug-induced toxicity. P9T PDO treatment and curve fitting were performed as in (A). Drug conditions with mixed cytostatic/cytotoxic phenotype reveal 10- to 20-fold higher IC_{50} values than assessed with the metabolic assay (A). Table summarizes drug IC_{50} values. Data are represented as means ± SD (of technical triplicate wells).

(E) Correlation plot comparing organoid viability scored by C scores and in-depth microscopic analysis (using PI as a dead cell marker). Dotted line represents linear regression curve, including 95% confidence intervals. Pearson correlation r = 0.94.

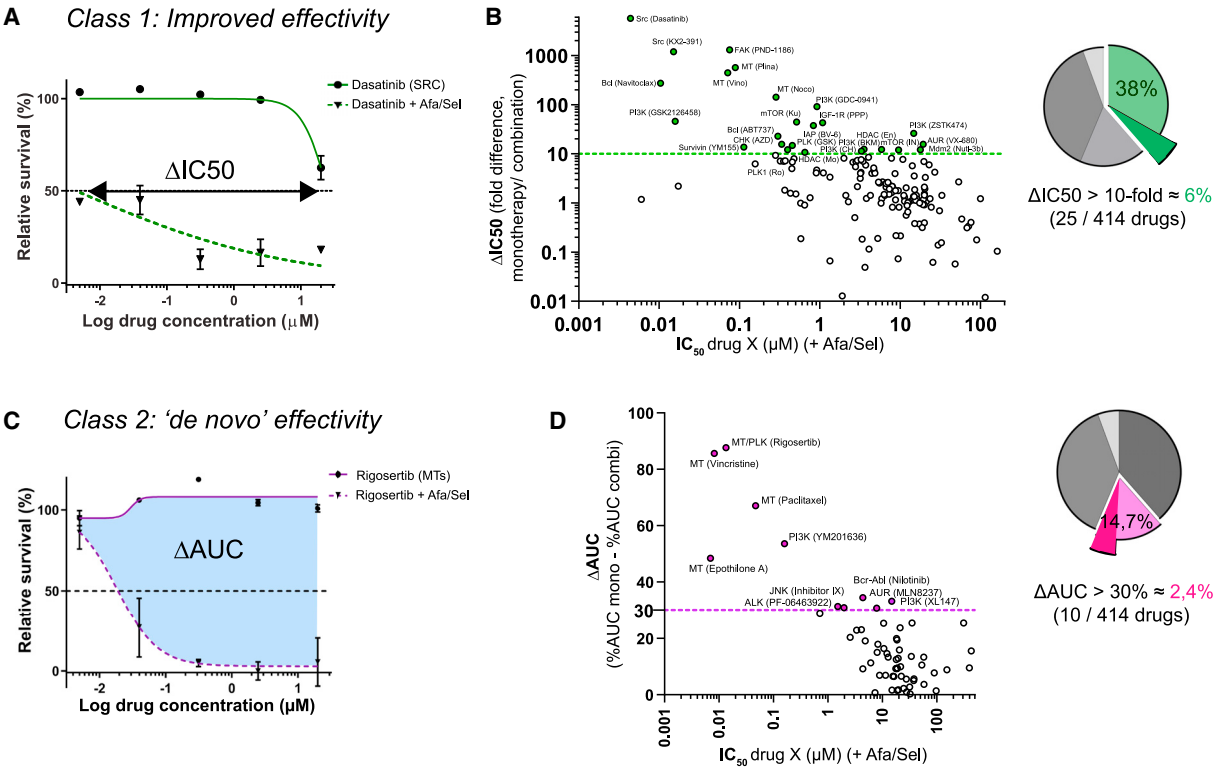

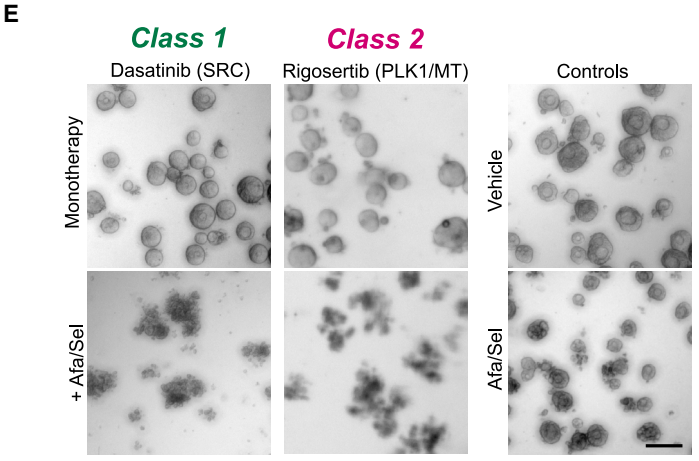

F

Summary of hits

Pathway	hits/group	%
Microtubule dynamics	9/11	**81,8**
Vinca alkaloids	2/2	
Taxanes	4/4	
Colchicine	3/5	
Apoptotic machinery	5/15	**33,3**
BCL-2	2/4	
Mdm2	1/7	
IAP-family	2/2	
PI3K/Akt/mTOR	9/36	**25,0**
PI3K	6/19	
mTOR	2/8	
PIKfyve	1/1	
Cell cycle	5/28	**17,9**
PLK	2/6	
Aurora kinase	2/7	
Chk	1/2	
non-receptor TKs	4/23	**17,4**
Src	2/4	
FAK	1/3	
Bcr/Abl	1/5	
p38/JNK MAPK	1/7	**14,3**
JNK	1/2	
Epigenetic regulation	2/24	**8,3**
HDAC	2/16	
RTK (non-HER)	2/43	**4,7**
IGF-1R	1/4	
ALK	1/1	

G

Drug	Consequence	MT target site	IC50 combi (μM)	ΔIC50 (fold)	ΔAUC (%)
Vincristine sulfate	destabilizing	Vinca	0,008		79,9
Vinorelbine tartrate	destabilizing	Vinca	0,071	447	
Paclitaxel (Taxol)	stabilizing	Taxane	0,047		66,9
Docetaxel (Taxotere)	stabilizing	Taxane	n.d.		45,6
Nocodazole	destabilizing	colchicine	0,285	142	
Plinabulin (NPI-2358)	destabilizing	colchicine	0,089	572	
Epothilone A	stabilizing	Taxane	0,007		49,1
Epothilone B (EPO906)	stabilizing	Taxane	n.d.		51,6
CYT997 (Lexibulin)	destabilizing	colchicine	0,282	9,3	
ABT-751	destabilizing	colchicine	18,055		13,0
Rigosertib (ON-01910)*	destabilizing	colchicine	0,014		82,1

(legend on next page)

(Figure 1C). We next performed side-by-side comparisons between our image-based analysis (Figure 1D) and the metabolic assay (Figure 1A). As expected, the estimated half-maximal inhibitory concentration (IC_{50}) values for cytostatic drugs (Afa, Sel, and their combination; Figure 1D) turned out to be 10- to 20-fold higher when interpreted through microscopic analysis of cell death. Only pure cytotoxic effects mediated by targeting the anti-apoptotic BCL-2 protein family with navitoclax (Nav) led to similar dose-response curves. Size analysis of organoids that survived drug treatment further underscored that low metabolic rates are easily misinterpreted as they can also represent cytostatic drug effects (Figure S1B).

Next, we validated our high-content imaging analysis (Figure 1D) with high-resolution confocal microscopy of individual organoids (Figure S1C). Reassuringly, C-score-based dead/alive classification of many PDOs in large cultures correlates ($r = 0.935$, $p < 0.05$) with scoring fractions of dead cells per organoid using PI incorporation (Figure 1E). Likewise, we found strong correlation between C score and fluorescent detection of additional apoptotic markers (Figures S1D–S1L).

Next, we confirmed the robustness of the C score being largely insensitive to organoid size and initial seeding density (for contemplations around these parameters, see STAR Methods) (Figures S2A–S2C). Moreover, the assay can be applied to other tissue-derived organoids, such as pancreatic ductal adenocarcinoma and non-small cell lung carcinoma (NSCLC) (Figures S2E and S2F), and multiple toxic compounds can serve as efficient positive controls (Figure S2D).

Importantly, our high-content assay detects a clear synergistic dose-response effect when titrating Nav in addition to low-dose (1 μM each drug) pan-HER/MEK combined inhibition (Figure 1D, dotted line), indicating that our setup has sufficient sensitivity to identify alternative Nav-like vulnerabilities to improve cytotoxicity of combinatorial pan-HER/MEK inhibition.

MTAs synergize with combined pan-HER/MEK inhibition

To identify therapeutic vulnerabilities in KRAS-mutant CRCs using PDO models, we used our high-content screening method to score drug-induced cell death on organoids to identify synergistic action with combined inhibition of EGFR/MEK pathway. CRC PDO P9T, a representative CRC model with *APC*, *KRAS*, and *TP53* driver mutations, was treated with a repurposing drug library consisting of 414 anti-cancer drugs that are either FDA-approved or in clinical trial. Reassuringly, scoring drug-induced cell death by our image-based assay was robust during the screen (Mean Z' factor of 0.68 ± SE 0.026). Next, dose-response curves were generated for all drugs, either as single agent or in combination with a fixed concentration of Afa/Sel (1 μM each) (Figures 2A and 2C). Effects of triplet combinations were normalized for moderate killing by Afa/Sel alone in order to expose synergism between a library drug and Afa/Sel over its actions as a monotherapy (Figure S3A). As expected,[17] a consistent and significant synergistic effect was identified upon Nav administration to Afa/Sel (mean 59-fold reduction in IC_{50} (Figure S3B).

For 38% of the library drugs, IC_{50} values could be established for both normalized dose-response curves (Figures 2A, 2B, and S4A). Within this category, 25 hits improved effectivity, defined by a >10-fold reduction in the IC_{50} (ΔIC_{50}) when the drug was combined with Afa/Sel (6% of library; Figures 2A and 2B; Table S1). Of note, inhibitors targeting the non-receptor tyrosine kinases (TKs) SRC (dasatinib [DASA] and KX2-391) and FAK (PND-1186) achieved high levels of synergy with Afa/Sel at concentrations in the nanomolar range (Figures 2A, 2B, and 2E; Table S1). Likewise, multiple MTAs (vinorelbine [VNRB], plinabulin, and nocodazole) demonstrated >100-fold reduction in the IC_{50} value (Figure 2B and Table S1). In addition, the vinca-alkaloid vinblastine and the SRC inhibitor SU6656 (neither present in the drug library) also showed a high degree of synergy with Afa/Sel (Figure S3C), further underscoring the potential of both drug targets.

Figure 2. Microtubule-targeting agents synergize with combined pan-HER/MEK inhibition

(A) Example of dose-response curve of dasatinib monotherapy (solid line) on PDO P9T (72 h) or in combination with Afa/Sel (both at 1 μM) (dashed line). IC_{50} values were obtained by non-linear regression fitting to a variable slope, normalized three-parameter model, using five drug concentrations. Normalization of individual curves was performed to their respective controls (further explained in Figure S3A). Triplet-drug combinations with improved efficacy are identified with a large shift in IC_{50}. Data are represented as means ± SD (of technical duplicates).

(B) Scatterplot summarizing the screening data on P9T PDO for compounds of which the ΔIC_{50} ($\Delta IC_{50} = (IC_{50\ monotherapy})/(IC_{50\ triplet\ combination})$ could be determined (38% of all drugs screened), where normalized (log−) IC_{50} values of the triplet therapy are plotted against their ΔIC_{50} values. ΔIC_{50} values >10 were classified as a hit in our screen and are marked in dark green (6% of all drugs).

(C) Example of dose-response curve of library compound (rigosertib) used as monotherapy (72 h), for which the IC_{50} could not be determined (solid line), and the combination with Afa/Sel (both at 1 μM) (dashed line). Drug treatment and curve fitting were performed as in (A). Compounds that demonstrate *de novo* efficacy are identified with large difference in area under the curve (ΔAUC) between both dose-response curves. Data are represented as means ± SD (of technical duplicates).

(D) Scatterplot summarizing the screening data on P9T PDO for compounds for which the ΔAUC was determined (14.7% of all drugs screened), where normalized (log−) IC_{50} values of the triplet therapy are plotted against their ΔAUC values. ΔAUC values >30% (= % $AUC_{monotherapy}$ minus % $AUC_{triplet\ combination}$) were classified as a hit in our screen and are marked in purple (2.4% of all drugs). Note that while MTAs docetaxel and epothilone B are clear hits based on ΔAUC values >30%, these are not depicted, as IC_{50} values of triplet therapy could not be determined.

(E) Representative images of P9T PDO exposed to indicated target hits and vehicle (DMSO) and Afa/Sel (both at 1 μM) controls, identified by either ΔIC_{50} or ΔAUC calculation. Monotherapy with the library drugs dasatinib (2.5 μM) and rigosertib (2.5 μM) (top row) showed no toxic effect (viable organoids are presented by typical cystic morphology), whereas their combination with Afa/Sel induced organoid death (bottom row). Scale bar, 200 μm.

(F) Table summarizing all hits per target, classified within functional groups (pathway inhibitors). The number of actual target hits per potential number of library hits is indicated.

(G) Table summarizing all the 11 microtubule-targeting agents that are screened. Indicated are their effects on microtubule dynamics, target site in the microtubule polymer, and their normalized IC_{50} (in the triplet combination), ΔIC_{50}, or ΔAUC values. Values represented by hits are indicated in green. *Rigosertib was recently classified as MTA.[34]

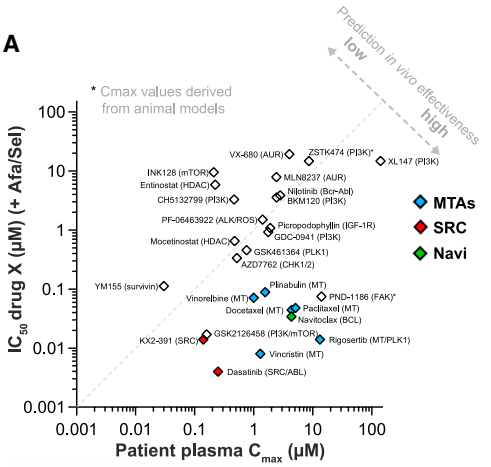

B

ΔAUC (%)

Drug	P9T	P6T	P16T	P26T	P18T-KRAS
MTAs					
Vinorelbine tartrate	51,9	44,6	68,1	25,4	35,6
Vincristine sulfate	85,6	47,4	78,8	46,4	29,0
Paclitaxel	67,0	56,2	35,9	15,7	18,9
Docetaxel	45,4	49,4	67,2	26,5	43,2
Rigosertib	87,7	40,1	48,9	35,0	13,4
Plinabulin	52,6	37,1	37,7	37,0	28,6
ABT-751	12,5	41,0	29,4	45,9	0,0
non-receptor TKs					
Dasatinib (Src)	71,1	35,9	69,9	24,5	35,8
KX2-391 (Src)	61,9	22,3	41,4	27,7	8,3
PF-573228 (FAK)	16,4	26,9	47,2	11,5	7,8
Apoptosis					
Navitoclax (Bcl2, Bcl-xL, Bcl-W)	60,4	34,2	46,1	14,2	54,3

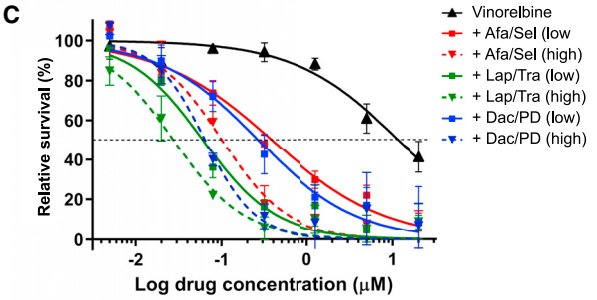

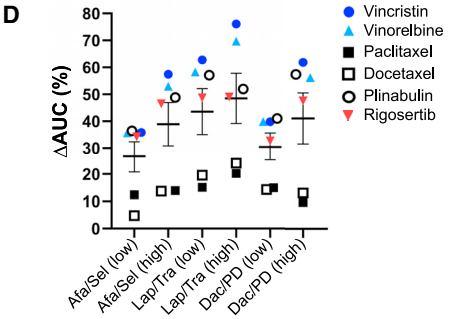

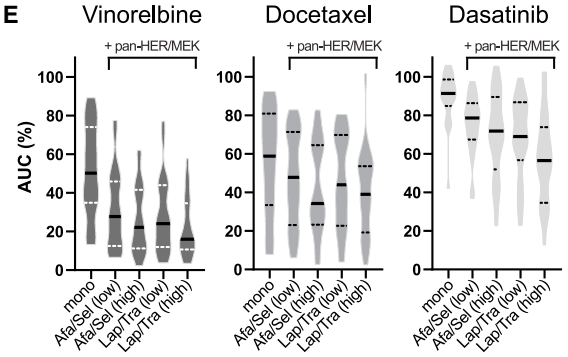

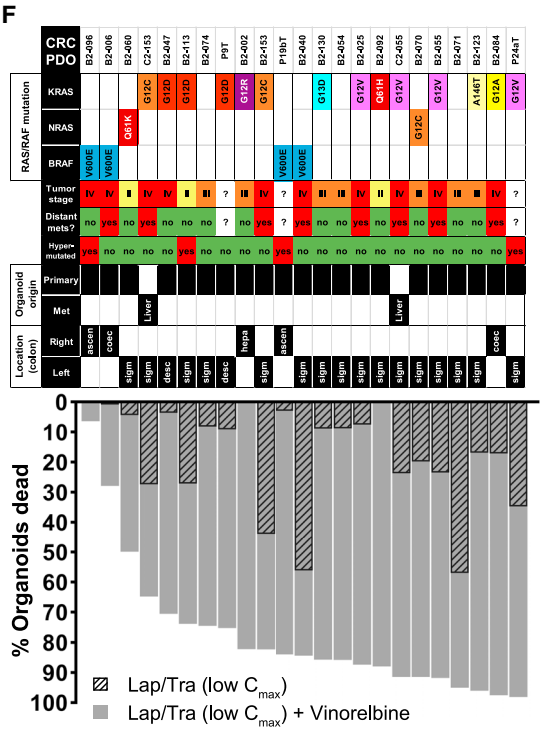

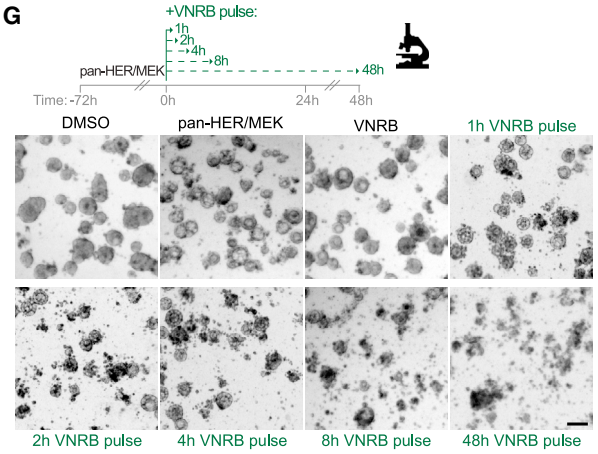

(legend on next page)

In the second category (14.7% of the library drugs), toxicity was only observed when combined with Afa/Sel (Figures 2C, 2D, and S4B; Table S1). As accurate ΔIC_{50} values could not be calculated for the monotherapy, we identified ten hits with "*de novo* effectivity" as defined by an area under the curve (AUC) reduction >30% (ΔAUC) when combined with Afa/Sel (2.4% of library, Figure 2D). Of these, the MTAs vincristine, paclitaxel, and epothilone A showed the highest degree of synergy with Afa/Sel. The same held true for top hit rigosertib (Figures 2C–2E), originally identified as a PLK1 inhibitor, but also described previously[34,35] and confirmed here (Figure S3D) to act as an effective microtubule (MT)-destabilizing agent. Multiple PI3K/mTOR inhibitors as well as cell-cycle checkpoint inhibitors were identified, albeit with lower synergy and lower overall IC_{50} values than the MTAs (Figure 2D and Table S1). In addition, 42% of the library drugs showed no cytotoxic effects within the range of concentrations tested (5 nM to 20 μM) (Table S2). Finally, few drugs were identified (4%) with clear effectivity as a single agent but without enhanced toxicity in the presence of Afa/Sel (Table S2).

To exclude non-specific effects, we reasoned that true vulnerabilities would be identified by drugs with common targets. Therefore, we subclassified the library drugs into functional groups per biological target or pathway and scored the prevalence of hits per group (Figure 2F). More than 80% (9 out of 11 drugs) of the MTAs was identified as a hit (Figure 2F), highlighting MTAs as the most potent group of drugs within our screen. Moreover, there seems to be no clear preference for the MT target site (vinca, taxane, or colchicine), nor for the effect on MT dynamics (Figure 2G).

pan-HER-MEK + MTA combination therapy demonstrates effective and uniform anti-tumor activity

To assess the therapeutic potential of any novel triplet-drug combination, we compared known patient plasma concentrations (C_{max}) for 27 out of 38 hits to their normalized IC_{50} values when combined with Afa/Sel (Figure 3A). Strikingly, all MTAs analyzed (marked in blue) were effective at IC_{50} concentrations >10-fold lower than patient C_{max}. Furthermore, both SRC inhibitors (DASA and KX2-391, marked in red) showed cytotoxicity-enhancing effects below C_{max} concentrations of patients. The FAK inhibitor (PND-1186) showed similar potential; however, multiple phase I trials using this drug were discontinued (ClinicalTrials.gov).

To exclude patient-specific effects, we further narrowed down our list of interesting hits by testing their efficacy on a panel of KRAS-mutant CRC PDOs (see Table S3). MTAs demonstrated most consistent effects across these PDOs when co-administered with Afa/Sel (Figures 3B and S3E). This was also true for ABT-751, which failed to make the cutoff during the initial screen on P9T PDOs but showed class-average efficacy on other KRAS-mutant PDOs. Of all other hits, SRC inhibitor DASA was like MTAs the most consistent across PDO models (Figure 3B).

Next, we compared the effects of different combinations of pan-HER/MEK inhibitors used in trials to treat RAS-mutant CRC, namely lapatinib (Lap)/trametinib (Tra), dacomitinib (Dac)/PD0325901 (PD), and Afa/Sel, at clinically relevant concentrations, i.e., the lowest (low) or highest (high) measured patient maximum plasma concentration (C_{max}).[9–11] Overall, in P9T PDOs we noticed strong synergy for all pan-HER/MEK combinations with the tested MTAs (Figures 3C and 3D), implying that

Figure 3. pan-HER/MEK + MTA combination therapy demonstrates effective and uniform anti-tumor activity

(A) Scatterplot comparing drug hits from PDO P9T screening data with the identified maximum plasma levels tolerated in patients (C_{max}). Normalized (log−) IC_{50} values from the indicated triplet combinations were used. Patient plasma C_{max} levels are estimated mean values from phase I trials (where ≥2 studies were included) corresponding to levels reached at the maximum tolerated dose or recommended phase 2 dose of the monotherapy. To be effective in patients, the *in vitro* IC_{50} value of a drug candidate should be at least lower than the *in vivo* C_{max}. Note that the IC_{50} value for docetaxel was estimated by applying a simplified non-linear regression model to the screen data. An asterisk indicates C_{max} level derived from animal studies.

(B) Table summarizing the validation of various drug screen hits on multiple KRAS-mutant CRC PDOs (n = 4). Data represent ΔAUC values (in percent) between dose-response curves of monotherapy and the respective triplet combination (as in Figure 2C). The validation screening method, curve fitting, and data normalization were performed similarly to the primary screen. For PDOs P6T, P16T, P26T, and P18T-KRAS the Afa/Sel concentrations were reduced to 250 nM to minimize their toxicity. Screening data are shown for PDO P9T. Green and red color hues indicate differences in efficacy (dark green shows highest efficacy, dark red the least). Arrowheads indicate compounds used for further studies.

(C) Dose-response curves of vinorelbine (VNRB) monotherapy on PDO P9T (for 72 h) or in combination with different combinations of pan-HER/MEK inhibitors at two clinically relevant concentrations (spanning the lowest [low] and highest [high] observed plasma C_{max} values in patients treated with these combinations). Curves were generated by non-linear regression fitting (using seven drug concentrations) upon normalization to the respective control conditions (similar to the screen). Data are represented as means ± SD (of three technical replicates). Dac, dacomitinib (pan-HERi); PD, PD-0325901 (MEKi).

(D) As in (C), dose-response curves were generated for six different MTAs in combination with three pan-HER/MEKi combinations at low and high C_{max}. Points indicate ΔAUC values (in percent) between MTA monotherapy and their combination with the indicated pan-HER/MEK inhibitors. Data means are shown for each HER/MEKi combination (±SD).

(E) Violin plots summarizing the effects of VNRB, docetaxel, and dasatinib on a panel of CRC PDOs (n = 23), either as monotherapy (mono) or as triplet combination with the indicated pan-HER/MEKi combination at low and high C_{max}. AUC values are relative to the respective normalized control (where AUC untreated = 1, or treated with pan-HER/MEKi = 1) and based on dose-response curves fitted as in (C). Violin plot shows full distribution of the data; thick black line indicates the median and thin lines the upper and lower quartile, respectively.

(F) Waterfall plot visualizing consistent triplet-combination-induced toxicities on the CRC PDOs panel. Clinical information per PDO is presented in the flanking table at the top, such as RAS/BRAF mutational status, tumor stage, metastases detected, PDO region of origin, and tumor location in colon. Bars indicate drug-induced organoid killing (absolute percentage) per PDO culture at low C_{max} of lapatinib (Lap)/trametinib (Tra) (1 μM and 7 nM, respectively) (striped bar) or in combination with VNRB at 120 nM (gray bar).

(G) Short-term exposure to VNRB (120 nM) in addition to continuous presence of Lap/Tra (high C_{max}, i.e., 3 μM + 22 nM). Additive exposure to VNRB as short as 8 h is sufficient to induce maximum cell death. Duration and scheduling of PDO P9T drug exposure as indicated. Representative images are shown (from duplicate wells). Scale bar, 100 μm.

functional suppression of the downstream MAPK pathway, rather than drug-specific effects, are synergistic with MT targeting. More specifically, Lap/Tra in combination with the vinca-alkaloids VNRB or vincristine was most effective (Figure 3D). As expected, this triplet-drug combination also outperformed the effectivity of VNRB with either Lap or Tra alone (Figures S3F and S3G). In the context of affordable healthcare, we also tested the combination of Lap with binimetinib (Bin), of which both patent families are or will soon start expiring (from 2020 to 2023 onward, respectively). As expected, all tested KRAS-mutant CRC PDOs demonstrated synergy with this Lap/Bin + VNRB combination at clinically relevant drug concentrations (Figures S3H and S3I). Notably, on primary and metastatic RAS-mutant CRC PDOs, we found no such synergy with other common first-line chemotherapeutics such as 5-fluorouracil, irinotecan (SN38) or oxaliplatin (Figures S5A and S5B).

We next tested the efficacy of the Afa/Sel and Lap/Tra combinations on a panel of 23 CRC PDOs using our image-based screening assay. Among the MTAs, we decided to continue with VNRB and docetaxel (DOCE). Both are FDA/European Medicines Agency-approved drugs, have favorable toxicity profiles in patients, and have expired patent registrations beneficial for affordable healthcare. Furthermore, these two MTAs manifest opposite MT targeting mechanisms (stabilizing vs. destabilizing). We also included DASA as the top hit from the non-receptor TKs. Assay robustness was high, with an average Z' factor of 0.80 ± SE 0.014). Overall efficacy of drug-induced cytotoxicity across 23 CRC PDOs are shown in violin plots that summarize the normalized AUC values for VNRB, DOCE, and DASA, either used as single agent or in combination with clinically relevant doses of Afa/Sel or Lap/Tra (Figure 3E). The triplet-drug combinations with VNRB showed most uniform effective killing of the CRC PDOs, irrespective of potential sensitivity to a single agent. Because of their similar target, PDO-specific responses to VNRB largely overlapped with DOCE (r = 0.91, Figure S5C), yet the synergistic effect of VNRB was superior over DOCE. Combination treatments of DASA with either Afa/Sel or Lap/Tra was overall the least effective, with significant variability between different PDOs (Figure 3E).

VNRB with Lap/Tra was most effective, showing a median killing effect of ~84% (with 19 of 23 CRC PDOs showing >70% of organoids killed) when Lap/Tra was applied at a low C_{max} (1 μM and 7 nM, respectively) in combination with the C_{max} of VNRB that is typically reached by oral dosing (120 nM) (Figure 3F). When VNRB concentrations of 1 μM are applied (approximate C_{max} upon intravenous dosing), median killing effect elevated to 93% (with 19 of 23 CRC PDOs showing >80% of organoids killed), compared with ~65% and ~38% median killing for DOCE and DASA, respectively (Figure S5D). Sensitivity of individual CRC PDOs to the triplet-drug combination did not depend on sensitivity to pan-HER/MEK inhibition (Figure 3F) or VNRB (Figure S5D) per se, indicating that the combination between VNRB and inhibition of the EGFR-RAS-MAPK pathway underlies the uniform anti-cancer activity across PDO models. Moreover, neither tumor stage (T2–T4), presence of metastases, hypermutation status, nor the presence of most CRC driver mutations were strong determinants for therapeutic response (Figures 3F and S6A). If any, PDOs isolated from right-sided CRCs were less sensitive for the triplet-drug combination, presumably because of their lower sensitivity toward pan-HER/MEK inhibition in general (Figures S6A and S6B). Enhanced resistance to anti-EGFR-based antibody therapy of right-sided CRC has also been described in the clinic.[36] Similarly, $BRAF^{V600E}$-mutant PDOs seemed slightly more resistant to the triplet combination at low concentrations of Lap/Tra (Figures S6A and S6C).

Patients are typically exposed to once-weekly administration of VNRB by intravenous injections.[37] To mimic such transient exposure in our PDO model, we pre-treated P9T organoids with Lap/Tra (high C_{max}) for 72 h prior to additional exposure to low-dose VNRB ranging from 1 to 48 h (Figure 3G). Near-instant cell killing was observed after VNRB administration, with exposures of 8 h or more showing the most extensive effects. Exposure to VNRB or Lap/Tra alone over the entire time course had minimal effect (Figure 3G). Regarding pharmacokinetics of VNRB, 8 h of exposure at 120 nM approximates the effective dose-concentration-time curves measured for VNRB in patients (where AUC ~ 1,059 ng h mL^{-1}).[38]

Clinically relevant therapy design in mice demonstrates superior anti-cancer activity of pan-HER/MEKi + VNRB

To investigate the potential clinical application of the triplet-drug combination, we tested its overall tolerability and anti-tumor efficacy in mice. A phase I/II clinical trial assessed Lap/Tra in patients with KRAS-mutant cancers, including CRC. This study established an optimal dosage schedule in patients using a 5-days-on/2-days-off drugs routine. Although disease stabilization was observed at best, prolonged pan-HER/MEKi treatment was well tolerated over multiple months.[9]

To mimic clinically relevant exposure in mice, we designed a treatment strategy to achieve *in vivo* drug concentrations and scheduling that reflects actual patient therapy. In particular, we explored administration of the drugs via the drinking water to achieve near-constant drug levels that is most reminiscent of pharmacokinetics in patients. For solubilized Tra we achieved a stable (mean) plasma concentration of ≈27.7 nM at steady state (day 24), which is near patient steady state (day 26, C_{max} levels of 25.51 nM) (Figure 4A). Administration of Lap through drinking water could not achieve correct levels, while daily oral gavage (50 mg/kg) was not well tolerated. Therefore, bidaily oral gavage (25 mg/kg twice a day) was applied that approximated patient plasma C_{max} to a close, albeit slightly lower level (0.69 μM vs. 2.4 μM, respectively).

Next, we applied the 5-days-on/2-days-off schedule to administer Lap/Tra and included mid-week injection with VNRB for two sequential weeks, interspersed with 1 week of rest in between cycles to mimic clinical use.[37] To test tolerability and efficacy of the triplet combination, P9T organoids were grafted subcutaneously into NOD-Scid gamma mice, and the tumor-bearing mice were treated when tumor volume reached ≥150 mm^3. Under treatment, average body weight as a measure of overall tolerability declined ≤14% but recovered partially during 2-day rest periods (Figure 4B). Almost full recovery was seen at the end of each cycle. Importantly, the triple-drug treatment showed no elevated toxicity in comparison with pan-HER/MEK targeting alone (Figure 4B). Next,

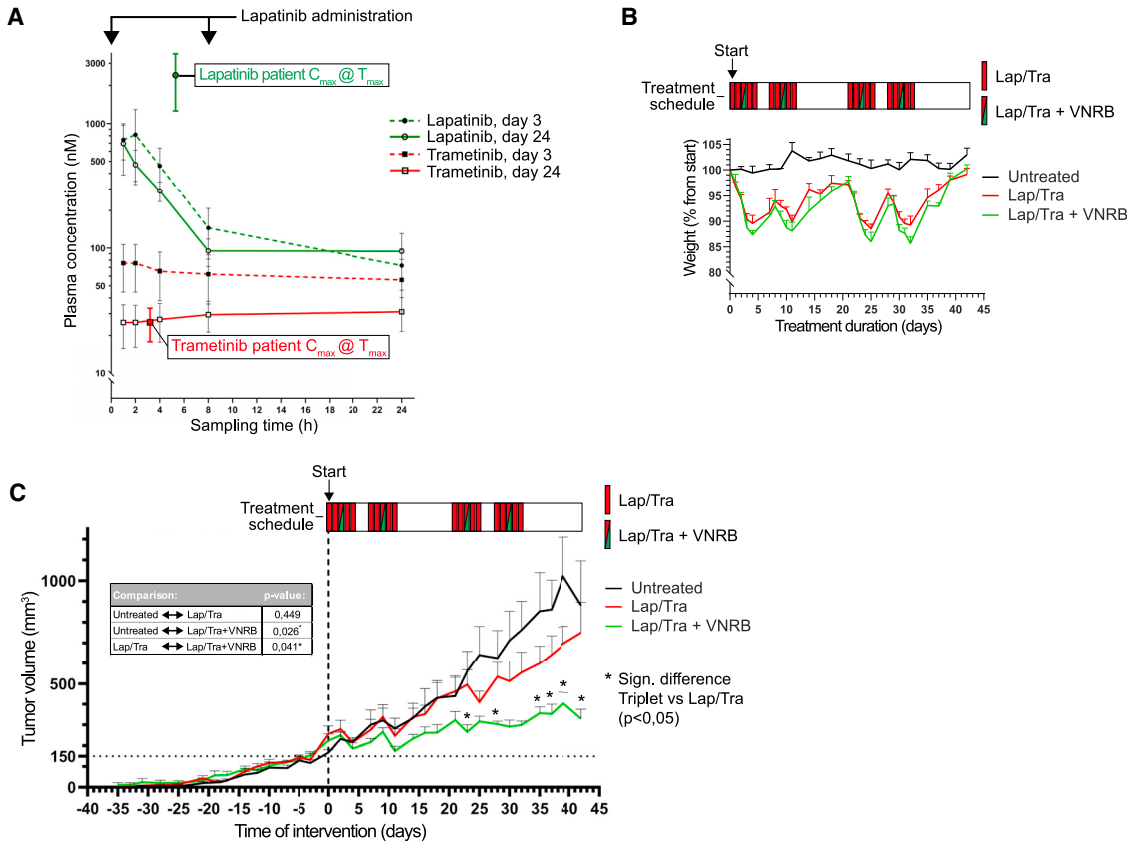

Figure 4. Clinically relevant therapy design in mice demonstrates enhanced anti-cancer activity of pan-HER/MEKi + VNRB

(A) Plasma concentration-time profile of Lap and Tra in NOD-Scid mice. Measurements were performed at day 3 (dashed line) and after 24 days (solid lines) of co-treatment with both drugs. Tra was administered via the drinking water (2.5 μg/mL), generating stable levels over time. Lap was dosed twice daily (oral gavage, 25 mg/kg and 12.5 mg/kg subsequently). Data are represented as means ± SD (four mice). In comparison, mean plasma C_{max} levels reached in patients for Lap (green filled circle) and Tra (red closed square) are indicated at the time (T_{max}) the C_{max} is reached (data from Huijberts et al.[9]).

(B) Body weight of control mice (black line) and mice that were exposed to Lap/Tra (red line) (5 days on, 2 days off), or the triplet combination (green line) including once-weekly (on day 3) VNRB (10 mg/kg intravenously). Treatment was given in cycles of 3 weeks with drug administration in weeks 1 and 2 prior to rest week 3 (as is common for VNRB monotherapy). In rest weeks 3 and 6, near complete recovery in body weight was observed. Data are represented as means ± SE (five mice per treatment arm).

(C) *In vivo* drug response of CRC PDO P9T, xenotransplanted subcutaneously in immunodeficient NOD-Scid mice. Treatment started once tumors reached approximately 150 mm^3. Treatment schedule with identical scheduling and concentrations as in (B). The change in absolute tumor volume is shown. Data are represented as means ± SE (five mice per treatment arm). The table depicts p values calculated by repeated-measures ANOVA. *p < 0.05.

two cycles of Lap/Tra + VNRB treatment repressed tumor growth with 62% compared with untreated mice (p = 0.032) and 55% compared with the mice that received Lap/Tra (p = 0.023, Figures 4C and S6D). Also, overall difference between the triplet combination and the other treatment arms were significant (table in Figure 4C). Moreover, while the additive effect of VNRB beyond Lap/Tra regarding tumor growth became most apparent during the second treatment cycle (Figure S6G), immunohistochemistry analysis of tumor epithelium indicated enhanced apoptosis as soon as 5 days after treatment (Figures S6E and S6F).

In conclusion, combining the fact that additive VNRB titration to pan-HER/MEK inhibitors can be both effective and tolerable at clinical drug levels *in vivo* together with the overall favorable drug sensitivity data of 23 PDO models that are generally considered to be patient representative (Emerens), further investigation is warranted in a phase I/II clinical trial to test its beneficial effect in patients (RASTRIC - EudraCT: 2019-004987-23).

Triplet-drug combination kills tumor cells at multiple stages of the cell cycle

MTAs can induce apoptosis in cycling cells through disturbance of MTs during spindle pole assembly, leading to prolonged mitotic arrest and, ultimately, death. Moreover, additional mechanisms have been described whereby MTAs target interphase MTs, thereby hampering cellular processes crucial for overall function and survival.[39] Pan-HER/MEK inhibition has been shown to induce a G_1 arrest in KRAS-mutant CRC PDOs,[17] suggesting that the enhanced cell death upon MTA addition can be induced in non-mitotic cells.

To decipher the exact mode of action of VNRB-induced cytotoxicity in pan-HER/MEK-treated cancer cells, we equipped P9T

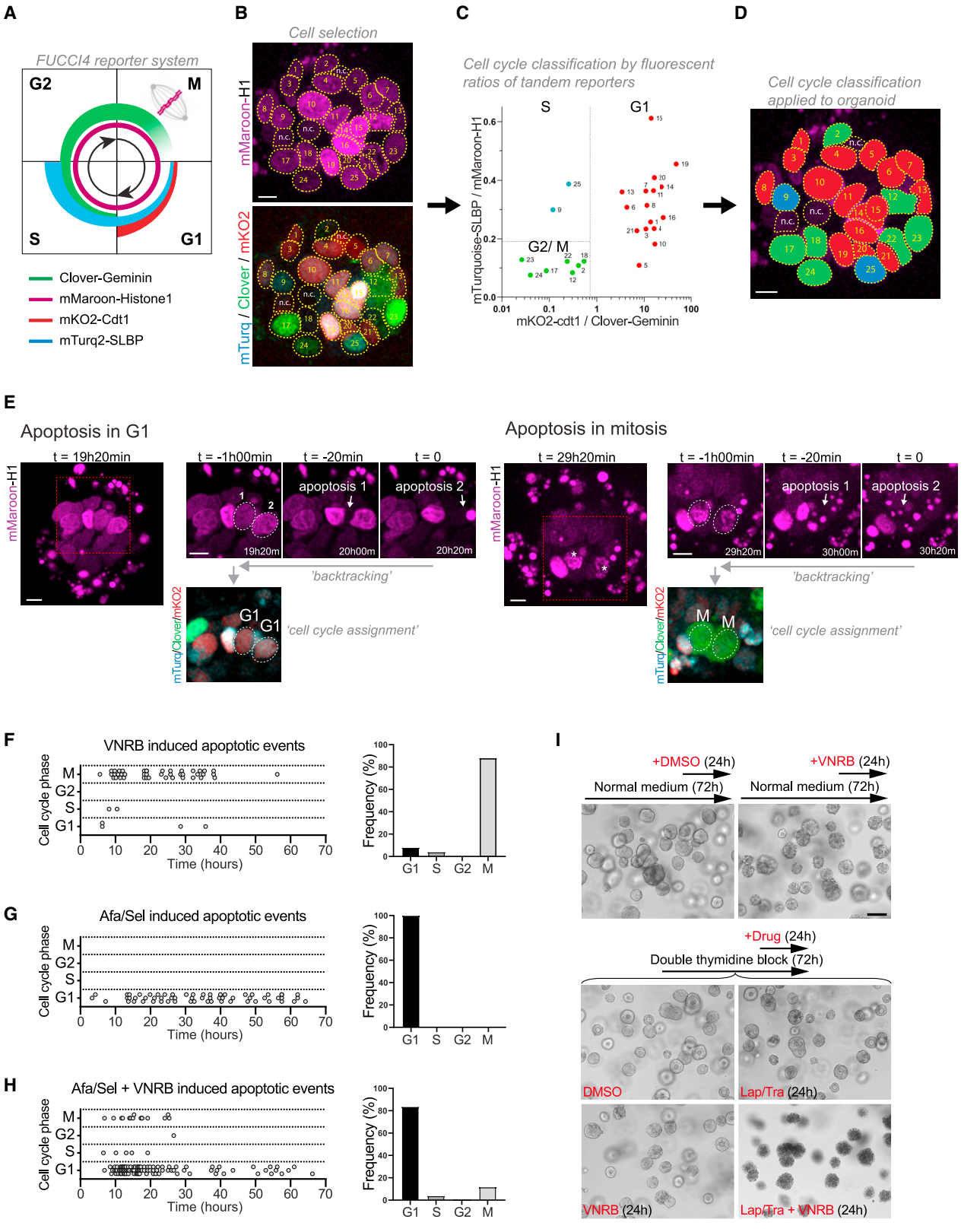

(legend on next page)

organoids with the FUCCI4 reporter system that labels each cell-cycle stage with a specific combination of fluorescent markers (Figure 5A).[40] Plotting the cell-specific ratios between these markers over time reveals the trajectory of cells along the cell cycle. Importantly, the time trajectory is not a necessity, as analyses of FUCCI4 marker ratios within a single time frame faithfully indicate cell-cycle status per cell (Figures 5B–5D, S7A, and S7B). Subsequently, within time-lapse imaging recordings of the drug-exposed organoids, we can "backtrack" apoptotic events in time (~1 h) to identify the cell undergoing that apoptotic event. Subsequent analysis of FUCCI4 markers in these cells reveals the cell-cycle stage in which drug-induced apoptosis was instigated (Figure 5E).

When we applied the above analysis to all apoptotic events that we could score during a 72-h drug response of P9T organoids with FUCCI4 sensors, we confirmed that VNRB as a single agent induces cell death in only few cells that were nearly all mitotic (Figure 5F). Similarly, drug-induced cytotoxicity by Afa/Sel was also incomplete, although apoptosis occurred predominantly in the G_1 phase of the cell cycle (Figure 5G). In contrast, the triplet-drug therapy eradicated nearly all tumor cells, and its effect could be subdivided into two phases. At the beginning of drug treatment (<30 h) apoptosis was triggered irrespective of cell-cycle stage, primarily being M and G_1 phase. Thereafter, cells died exclusively during the G_1 phase of the cell cycle (Figure 5H), presumably as these remaining cells became first G_1-arrested due to Afa/Sel. The same mode of drug response was confirmed in three additional PDO lines where cell killing by the triplet combination was also not dependent on mitosis (Figure S7C).

To confirm that the mode of action of the triplet-drug combination synergizes in G_1 cells and is independent of drug-induced defects in the previous mitosis, we kept P9T organoid cells arrested at the G_1/S-phase boundary of the cell cycle by a double-thymidine block (Figure S7B) and tested their response to either pan-HER/MEK inhibition, VNRB, or their combination. As expected, the triplet-drug combination induced maximum toxicity in G_1/S-arrested cells, while both Afa/Sel or VNRB independently showed no effect (Figure 5I).

Mechanistic insight into the synergy of the triplet-drug combination

Combined MEK inhibition and MTA treatment has previously been suggested to drive apoptosis in CRC cell lines by changing the balance between pro-apoptotic BIM and anti-apoptotic MCL1.[41] Using multiple KRAS-mutant CRC PDOs, we here confirm upregulation of BIM as a consequence of pan-HER/MEK inhibition with Lap/Tra (Figures 6A and S8A), while cleaved MCL1 was only observed as a result of the triplet-drug combination that induces maximum apoptosis. However, while the pan-caspase inhibitor ZVAD-fmk fully blocked the loss of MCL1 (lane 5), it could not prevent apoptosis (data not shown), indicating that MCL1 inhibition may facilitate cell death induction but is unlikely to be the primary trigger. The induction of BIM, as a consequence of MAPK pathway inhibition, could also be observed in lysates from treated CRC PDO xenografts in mice (Figure S8C). In addition to KRAS-mutant lines, we tested other CRC PDOs with NRAS, BRAF, or without activating mutations in the MAPK-signaling pathway (Figure S8B). However, while induction of apoptosis was apparent, we found no strict correlation with BIM induction, suggesting that apoptosis is not the direct result of BIM induction through MAPK inhibition.

Alternatively, anti-apoptotic proteins of the BCL2-family are influenced by both the MAPK-signaling pathway and MT integrity.[42] To pinpoint whether individual BCL2-family members counteract the elevated pro-apoptotic BIM levels in organoids, we scored the effect of their individual inhibition in combination with Lap/Tra using PDO P9T (Figure 6B). In line with earlier results, co-targeting of BCL-xL via Nav (BCL2, BCL-xL, and BCLw inhibitor) or WEHI-539 (specific BCL-xL inhibitor) was detrimental for cell survival when combined with Lap/Tra

Figure 5. Triplet combination kills tumor cells at all stages of the cell cycle

(A–D) Accurate cell-cycle identification in living CRC PDOs using FUCCI4 reporter system. (A) Cell-cycle scheme showing four fluorescent reporters, each exclusive to specific phases of the cell cycle. Measuring the intensity ratios of two tandem reporters by time-lapse microscopy, combined with the visualization of chromatin condensation and separation (by mMaroon-H1) during mitosis, allow for identification of the cycle stage of individual cells. (B) Representative (z-projected) image of PDO P9T with stable genomic integration of FUCCI4 reporters. The uniform presence of mMaroon-H1 (purple, upper panel) allowed segmentation of individual nuclei, used to mask and measure fluorescent intensity of mMaroon and the three additional reporters (overlay, lower panel). Cells with mMaroon fluorescent intensity <3× background intensity were not considered (n.c.) for analysis. (C) Scatterplot presenting cellular FUCCI4 ratios of cells identified in (B). Setting fluorescent "ratio gates" (dotted lines), defined by tracking of reference G_2/M cells with high confidence (see Figure S6A and STAR Methods), allowed accurate cell-cycle classification of the indicated cells in three groups (G_1, orange; S, blue; G_2/M, green). Further discrimination between G_2 and M cells was performed by chromatin phenotype. (D) Cell-cycle stage classification from (C) applied to the depicted organoid from (B). Scale bar, 10 μm.

(E) Identification of cell-cycle phase prior to triplet-induced cell death in CRC PDO using "backtracking" of the apoptotic events in time. Representative stills from live-cell-recorded drug response on two P9T organoids. Left: organoid with zoom panels show backtracking of two apoptotic events to cells to which cell-cycle phase was assigned to be G_1. Right: organoid with zoom panels show backtracking of two apoptotic events to cells at M phase of the cell cycle. Asterisks mark cells with condensed chromosomes, early in mitosis. Scale bars, 10 μm.

(F) FUCCI4-based cell-cycle analysis of apoptotic events during drug response of PDO P9T exposed to VNRB (120 nM). Along the duration of the drug response (x axis), apoptotic events were scored and classified per antecedent cell-cycle phase (y axis, left panel). VNRB induces cytotoxicity predominantly in mitotic cells (right panel). n = 50 dead cells over five organoids.

(G) Similar to (F), but now during drug response to the Afa/Sel combination (both at 1 μM). In contrast to VNRB, the Afa/Sel combination induces apoptosis in the G_1 phase of the cell cycle (right panel). n = 60 dead cells over five organoids.

(H) Similar to (F), but now during drug response to the triplet-drug combination. Cell death was induced at multiple stages of the cell cycle, but with a strong bias toward G_1 (right panel). n = 128 dead cells over seven organoids.

(I) Disruption of MT integrity by VNRB efficiently kills G_1/S-arrested cells when the EGFR/MAPK pathway is inhibited. Representative bright-field images of control and drug-treated P9T organoids, growing under normal conditions (upper panels) or G_1/S arrested through a double-thymidine block (lower panels). Organoids were briefly challenged (as indicated) with VNRB (120 nM), Lap/Tra (high C_{max}), or the triplet combination. Scale bar, 100 μm.

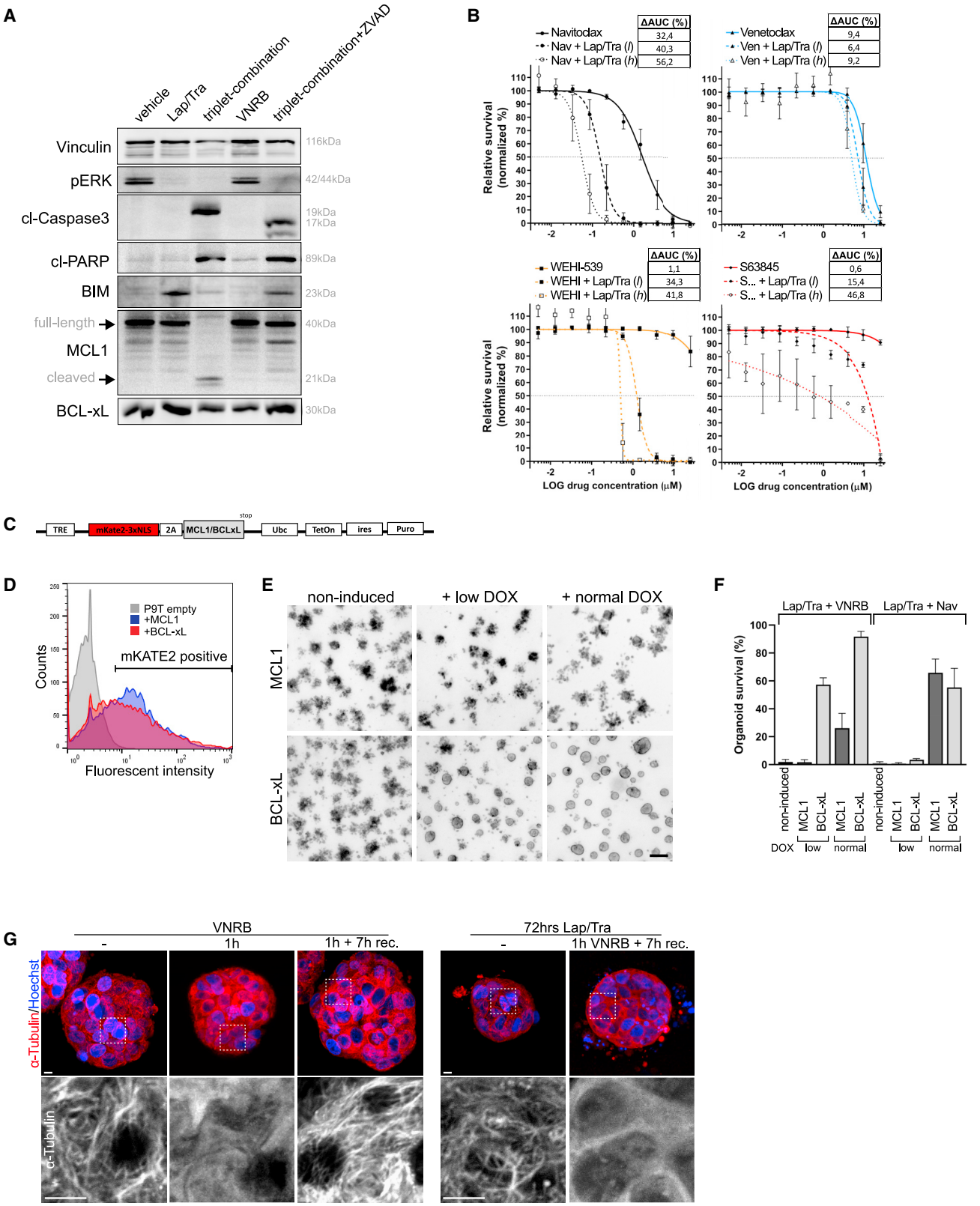

(legend on next page)

(Figure 6B),[16,17] while the BCL2 inhibitor venetoclax showed no such effect. Targeting MCL1 with S63845 demonstrated only minor synergy when combined with the high C_{max} of Lap/Tra (Figure 6B).

To confirm that BCL-xL activity is compromised during triplet-drug treatment, we tested a rescue experiment by inducible expression of BCL-xL or MCL1 (coupled to red fluorescent mKate2 as a control) (Figures 6C and 6D). Indeed, inducing BCL-xL levels effectively neutralized triplet-drug-induced apoptosis, supporting a model wherein VNRB, alone or in combination with pan-HER/MEK inhibition, counteracts BCL-xL activity (Figures 6E and 6F). In contrast, inducing MCL1 levels was far less efficient in rescuing triplet-drug-induced cytotoxicity (Figure 6F). The actions of MCL1 therefore appear to be downstream of the drug combination's primary inactivation of BCL-xL.

Lastly, we tested whether part of the synergy between EGFR-MAPK pathway inhibition and VNRB treatment could be explained by enhanced disturbance of the MT network. The rapid and reversible effects of VNRB on MT disturbance were consistent in multiple tested PDOs, yet for two sensitive CRC PDOs we again found that continuous pan-HER/MEK inhibition prohibited MT restoration once VNRB treatment was stopped, thereby prolonging the downstream effects initially triggered by a VNRB pulse (Figures 6G and S8D). Notably, the Afa/Sel-insensitive CRC PDO P26T showed the least restoration defects, potentially contributing to its relative resistance to the triplet-drug combination (Figure S8D).

DISCUSSION

Drug-sensitivity tests on PDOs are highly anticipated to become implemented in personalized anti-cancer care. Moreover, great potential is attributed to pre-clinical drug screens on PDOs to facilitate drug discovery and therapy development. Here, we employed PDOs of KRAS-mutant CRC to exploit its potential as a screening platform to identify targetable vulnerabilities that become exposed during existing therapies that otherwise remain incomplete. We chose to improve therapeutic combination strategies that co-target EGFR and MEK in KRAS-mutant CRC. Different EGFR/MEK-targeting studies have recently been completed and have shown that strong suppression of downstream ERK activity could be achieved within tolerable dosing regimens.[9–11] Temporary stabilization of tumor volume was observed but, unfortunately, disease progressed over time. The failure of these drugs to induce cytotoxicity[17] likely explains the limited therapeutic efficacy and was the rationale for the current triplet-combination screen.

To correctly score drug-induced cytotoxicity in PDO cultures, we implemented a high-content imaging screen to discriminate cell death in organoid cultures from cytostatic states, as the latter's dormant metabolic nature is often misinterpreted as death by ATP or REDOX-based viability assays.[17] Our phenotypic analysis is based on circularity of an organoid structure, a single and robust parameter that reliably identified drug-induced cytotoxicity (Z' factor of 0.68). The circularity phenotype can be captured using standard microscopy equipment and should be widely applicable. Moreover, improving automatic object identification and phenotypic classification, including additional parameters, provides room to facilitate higher throughput and/or multiplexed readouts. Stringent filtering of the screen data of a library of 414 anti-cancer drugs yielded 34 positive hits. Their validation on a small set of KRAS-mutant PDOs demonstrated no false positives, underscoring the reliability of the screening assay. The type of negative hits and false-negative rate was not assessed but is likely influenced by drugs not reaching target concentration (>20 μM) or effective exposure time (maximum 72 h in our screen).

Using our drug-repurposing screen on KRAS-mutant CRC PDOs, MTAs were identified as the most potent class of compounds (9 out of 11 drugs). This class includes vinca-alkaloids,

Figure 6. Mechanistic insight into the synergy of the triplet-drug combination

(A) Western blot analysis on lysates of drug-challenged PDO P9T. Organoids were pre-treated for 72 h with vehicle (lanes 1 and 4) or Lap/Tra (high C_{max}, lanes 2, 3, and 5), then treated as indicated for another 24 h, followed by harvesting. Treatment with Lap/Tra induced pro-apoptotic BIM expression, while co-administration of VNRB (120 nM) triggered apoptosis and MCL1-cleavage. Pan-caspase inhibitor ZVAD prevented MCL1 cleavage but could not stop drug-induced cytotoxicity. Cl-Casp3, cleaved (active) caspase 3; Cl-PARP, cleaved (active) poly(ADP-ribose) polymerase.

(B) Dose-response curves of PDO P9T treated with the indicated inhibitors targeting several BCL2 family members. Curves represent monotherapy (solid line), or combinations Lap/Tra at low (dashed line) or high (dotted line) patient C_{max}. Navitoclax (inhibiting BCL2, BCL-xL, and BCL-W) and WEHI-539 (BCL-xL inhibitor) displayed synergy with pan-HER/MEK inhibition, in contrast to the BCL2-specific inhibitor venetoclax. The MCL1 inhibitor S63845 displayed synergy, but predominantly in combination with high C_{max} dose of Lap/Tra. Curves were generated by non-linear regression fitting (using ten drug concentrations) upon normalization to the respective control conditions. ΔAUC values display differences between monotherapy curves and the indicated curves. Data are represented as means ± SD (of three technical replicates).

(C–F) Anti-apoptotic BCL-xL protects against the cytotoxic effect of the triplet-combination. (C) Schematic of lentiviral construct used to achieve doxycycline (DOX)-inducible expression of MCL1 or BCL-xL. Expression can be monitored via simultaneous co-expression of fluorescent mKate2, separated from MCL1/BCL-xL via a P2A peptide sequence. (D) Fluorescence-activated cell sorting analysis of mKate2 fluorescence on PDO P9T, stably expressing inducible MCL1/BCL-xL constructs. Induction with a low concentration DOX showed identical expression. (E) Representative bright-field images of PDO P9T cultures treated for 72 h with the triplet combination (high C_{max} Lap/Tra +120 nM VNRB), with or without induction (including 24 h pre-induction) of MCL1 (upper panels) or BCL-xL (lower panels) expression, at both low and high DOX levels. Drug-induced cytotoxicity was predominantly counteracted via BCL-xL, but not MCL1. Scale bar, 100 μm. (F) Manual quantification of drug-induced cytotoxicity of the experiment in (E), including organoids treated with a triplet-drug combination of Lap/Tra (high C_{max}) with navitoclax (1 μM). Data are represented as means ± SE (three independent biological replicates, each consisting of an average of technical duplicate wells).

(G) Representative (z-projection) confocal images of PDO P9T cultures, fixed and stained for α-tubulin to visualize MT integrity (red in top row, gray in bottom row for maximum contrast) and nuclei (Hoechst 33342, blue in top row). Organoids were pre-treated for 72 h with vehicle (left three columns) or Lap/Tra (high C_{max}, right two columns). Subsequently, organoids were treated with VNRB (120 nM) for 1 h and fixed (second column) or followed by a washout and 7 h recovery (rec.) prior to fixation (columns 3 and 5). Continuous suppression of the MAPK pathway casted long-lasting effects of VNRB-triggered MT destabilization (compare column 3 with column 5). Scale bars, 5 μm.

colchicines (both MT destabilizing), and taxanes (MT stabilizing) with diverse mechanisms of action against MTs, highlighting MT network integrity as the vulnerable co-target during inhibition of the EGFR-RAS-MAPK pathway. Notably, three additional screen hits, JNK inhibitor IX (JNK), picropodophyllin (IGF-1R), and BKM120 (pan-PI3K) have also been shown to exert MT-destabilizing activity.[43–45] Of all possible MTA drug candidates, we selected VNRB as our most promising hit. Foremost, vinca-alkaloids demonstrated more uniform effects across multiple PDOs than taxanes, VNRB is a non-proprietary chemotherapeutic regularly used to treat multiple cancer types and, lastly, extensive clinical expertise with VNRB indicates a more favorable toxicity profile than vincristine.

There is an ongoing debate regarding the mode of action of MTAs against tumors *in vivo*.[46,47] Classically, MTAs were anticipated to target proliferative tumor cells by disrupting proper mitotic spindle formation, but accumulating evidence suggests a role in non-dividing cells as well. At the molecular level, the processes related to MTA-induced mitotic catastrophe and death upon mitotic slippage have been extensively studied and imply that the balance between anti-apoptotic BCL-xL, MCL1, and pro-apoptotic BIM ultimately define cell fate.[48–50] Drugs influencing this balance directly, as shown for Nav,[50] or indirectly, could therefore act synergistically with MTAs to induce mitotic cell death. Indeed, the cytotoxic action of MTAs combined with the MEK inhibitor PD0325901 relies on mitotic arrest and BIM upregulation in CRC cell lines.[41]

Importantly, MTAs can also induce cancer cell death in interphase,[51,52] including VNRB in CRC cell lines.[53] Using live-cell imaging of CRC PDOs expressing cell-cycle reporters, we were able to couple the moment of apoptotic events in drug-challenged organoids to the cell-cycle state at which it occurred. As expected, the limited cell death observed upon VNRB monotherapy was confined to M phase. However, the triplet-combination therapy induced cytotoxicity at multiple phases of the cell cycle, with a strong bias toward G_1. Inducing apoptosis in tumor cells irrespective of their proliferative nature is crucial because large fractions of tumors consist of non-proliferative cells. The specific role of apoptotic proteins in MTA-driven cell death during interphase is more elusive than during mitosis, although functional BIM seems necessary for this process in CRC cells.[53] In agreement with other reports using cell lines, BIM was upregulated in response to MAPK pathway inhibition in our PDO cultures. Our data suggest that BCL-xL and to a lesser extent MCL1 can neutralize apoptotic priming by upregulated BIM, but that this function is directly or indirectly counteracted by disturbances of the MT network, ultimately leading to apoptosis. How stress on the interphase MT network translates into BCL-xL/MCL1 inhibition at the molecular level remains unexplored at this point.

The main dose-limiting toxicity of VNRB (and MTAs in general) therapy is bone marrow suppression. Exposing PDO cultures to a clinically relevant pulse of VNRB initiated only a transient, non-lethal disruption of the MT network. However, simultaneous inhibition of the EGFR-RAS-MAPK pathway sustained MT network disruption triggered by a VNRB pulse. It is conceivable that in contrast to direct and uniform targeting of the BCL-xL-mediated apoptotic machinery, the indirect inhibition of BCL-xL by VNRB-pan-HER/MEK inhibition becomes restricted to epithelial tissues and cancers due to the expression pattern of EGFRs. Indeed, the triplet-combination therapy is tolerated equally well *in vivo* as combined pan-HER/MEK inhibition.

Despite encouraging pre-clinical data regarding the anti-tumor effects of classical MTAs in CRC, minimal clinical effects of vinca-alkaloid[54] and taxane[55] monotherapies have been observed, presumably discouraging further exploration of their combinatorial use with targeted inhibitors in CRC. However, effective co-targeting has been described for several other cancer indications. Combination therapy with trastuzumab, pertuzumab (antibodies targeting HER2), and docetaxel are standard care for first-line treatment of HER2-positive metastatic breast cancer,[56] and the combination of Lap and VNRB is an active and well-tolerated regimen for this patient group as well.[57] Furthermore, EGFR-positive NSCLC patients could benefit from second-line therapy consisting of combinations of docetaxel with EGFR inhibitors erlotinib or gefitinib.[58]

We demonstrate here the consistent efficacy of VNRB-pan-HER/MEK inhibition across >20 CRC PDOs that is independent of RAS mutational status. Moreover, anti-tumor effects remained unaffected when the EGFR/MEK inhibitors were replaced by different, but mechanistically identical drugs, provided that downstream MAPK pathway signaling was effectively inhibited. Of interest regarding affordable healthcare, we successfully combined VNRB with the targeted inhibitors Lap (pan-HER) and binimetinib (MEK), both patent families of which are first to expire in relation to their competitors. A phase I/II clinical trial to test the beneficial effect of this triplet combination in patients with metastatic RAS-mutant CRC has been started (RASTRIC - EudraCT: 2019-004987-23). Recently, novel EGFR-RAS-MAPK pathway inhibitors have been developed, for instance by specifically targeting mutant $KRAS^{G12C}$ or using tumor-specific antibodies against EGFR.[31,59] Although improved tumor specificity is expected, we advocate that these novel therapies might still gain additional anti-tumor activity from co-administration of VNRB, a commonly used drug in clinical oncology.

Limitations of the study

Our ultimate goal was to apply a robust high-throughput screening methodology to identify a targetable vulnerability in a human cancer. We chose to apply a screening strategy that maximizes efficiency at the expense of generating a well-balanced resource-like dataset. Indeed, we deliberately screened the whole drug library on only one PDO model and immediately entered multiple rounds of follow-up assays with only those hits that continuously passed stringent filters. As a result, we reduced time and resources spent on negative hits, while high-potential drug candidates still became extensively validated in multiple models and experimental setups. The negative consequence is the lack of follow-up on early negative data in the initial screen, yielding inherent low confidence in these values.

STAR★METHODS

Detailed methods are provided in the online version of this paper and include the following:

SUPPLEMENTAL INFORMATION

Supplemental information can be found online at https://doi.org/10.1016/j.celrep.2023.112324.

ACKNOWLEDGMENTS

We thank all lab members for reagents, suggestions, and discussions. We thank Prof. Dr. O. Kranenburg (Department of Surgical Oncology, UMC Utrecht Cancer Centre) for providing TOR PDOs. This work is funded by the Gravitation Program "CancerGenomics.nl" from the Netherlands Organization for Scientific Research (NWO), a grant from the Dutch Cancer Society (KWF/UU2013-6070 to H.J.G.S.), an ERC starting grant (IntratumoralNiche to H.J.G.S.), a KWF/Alpe d'HuZes grant (J.L.B. and H.C.), and a "Stand Up to Cancer" International Translational Cancer Research grant (J.L.B. and H.C.). Stand Up to Cancer is a program administered by the American Association for Cancer Research. The Mouse Clinic for Cancer and Aging (N.P., O.v.T., and M.v.d.V.) is supported by National Roadmap grant for Large-Scale Research Facilities of the Netherlands Organization for Scientific Research (NWO). The Oncode Institute is partly financed by the Dutch Cancer Society.

AUTHOR CONTRIBUTIONS

H.C., J.L.B., and H.J.G.S. conceived the project. S.M. and H.J.G.S. designed experiments. S.M., M.A.H., C.S.V., B.P., R.O., and H.B. performed experiments. N.P., O.v.T., and M.v.d.V. performed mouse experiments. S.M., S.F.B., J.M.L.R., and H.J.G.S. analyzed data. S.M. and H.J.G.S. wrote the manuscript.

DECLARATION OF INTERESTS

S.M., C.S.V., J.L.B., and H.J.G.S. are inventors on a patent concerning the combination of MTAs with targeted inhibition of the EGFR-MAPK-signaling pathway. C.S.V., R.O., and S.F.B. are employed by Hubrecht Organoid Technology, which holds the exclusive license to the organoid technology. H.C. is an inventor of several patents related to organoid technology; his full disclosure is given at https://www.uu.nl/staff/JCClevers/.

Received: March 2, 2021
Revised: January 6, 2023
Accepted: March 17, 2023
Published: March 30, 2023

REFERENCES

1. Ryan, M.B., and Corcoran, R.B. (2018). Therapeutic strategies to target RAS-mutant cancers. Nat. Rev. Clin. Oncol. *15*, 709–720. https://doi.org/10.1038/s41571-018-0105-0.
2. Yaeger, R., and Corcoran, R.B. (2019). Targeting alterations in the RAF-MEK pathway. Cancer Discov. *9*, 329–341. https://doi.org/10.1158/2159-8290.CD-18-1321.
3. Karnoub, A.E., and Weinberg, R.A. (2008). Ras oncogenes: split personalities. Nat. Rev. Mol. Cell Biol. *9*, 517–531. https://doi.org/10.1038/nrm2438.
4. Yao, Z., Torres, N.M., Tao, A., Gao, Y., Luo, L., Li, Q., de Stanchina, E., Abdel-Wahab, O., Solit, D.B., Poulikakos, P.I., and Rosen, N. (2015). BRAF mutants evade ERK-dependent feedback by different mechanisms that determine their sensitivity to pharmacologic inhibition. Cancer Cell *28*, 370–383. https://doi.org/10.1016/j.ccell.2015.08.001.
5. Corcoran, R.B., André, T., Atreya, C.E., Schellens, J.H.M., Yoshino, T., Bendell, J.C., Hollebecque, A., McRee, A.J., Siena, S., Middleton, G., et al. (2018). Combined BRAF, EGFR, and MEK inhibition in patients with BRAF(V600E)-mutant colorectal cancer. Cancer Discov. *8*, 428–443. https://doi.org/10.1158/2159-8290.CD-17-1226.
6. van Geel, R.M.J.M., Tabernero, J., Elez, E., Bendell, J.C., Spreafico, A., Schuler, M., Yoshino, T., Delord, J.P., Yamada, Y., Lolkema, M.P., et al. (2017). A phase ib dose-escalation study of encorafenib and cetuximab with or without alpelisib in metastatic BRAF-mutant colorectal cancer. Cancer Discov. *7*, 610–619. https://doi.org/10.1158/2159-8290.CD-16-0795.
7. Kopetz, S., Grothey, A., Yaeger, R., Van Cutsem, E., Desai, J., Yoshino, T., Wasan, H., Ciardiello, F., Loupakis, F., Hong, Y.S., et al. (2019). Encorafenib, Binimetinib, and cetuximab in BRAF V600E-mutated colorectal cancer. N. Engl. J. Med. *381*, 1632–1643. https://doi.org/10.1056/NEJMoa1908075.
8. Yaeger, R., Weiss, J., Pelster, M.S., Spira, A.I., Barve, M., Ou, S.I., Leal, T.A., Bekaii-Saab, T.S., Paweletz, C.P., Heavey, G.A., et al. (2022). Adagrasib with or without cetuximab in colorectal cancer with mutated KRAS G12C. N. Engl. J. Med. *388*, 44–54. https://doi.org/10.1056/NEJMoa2212419.
9. Huijberts, S.C.F.A., van Geel, R.M.J.M., van Brummelen, E.M.J., Opdam, F.L., Marchetti, S., Steeghs, N., Pulleman, S., Thijssen, B., Rosing, H., Monkhorst, K., et al. (2020). Phase I study of lapatinib plus trametinib in patients with KRAS-mutant colorectal, non-small cell lung, and pancreatic cancer. Cancer Chemother. Pharmacol. *85*, 917–930. https://doi.org/10.1007/s00280-020-04066-4.
10. van Brummelen, E.M.J., Huijberts, S., van Herpen, C., Desar, I., Opdam, F., van Geel, R., Marchetti, S., Steeghs, N., Monkhorst, K., Thijssen, B., et al. (2021). Phase I study of Afatinib and Selumetinib in patients with KRAS-mutated colorectal, non-small cell lung, and pancreatic cancer. Oncologist *26*, 290–e545. https://doi.org/10.1002/onco.13631.
11. van Geel, R.M.J.M., van Brummelen, E.M.J., Eskens, F.A.L.M., Huijberts, S.C.F.A., de Vos, F.Y.F.L., Lolkema, M.P.J.K., Devriese, L.A., Opdam, F.L., Marchetti, S., Steeghs, N., et al. (2020). Phase 1 study of the pan-HER inhibitor dacomitinib plus the MEK1/2 inhibitor PD-0325901 in patients with KRAS-mutation-positive colorectal, non-small-cell lung and pancreatic cancer. Br. J. Cancer *122*, 1166–1174. https://doi.org/10.1038/s41416-020-0776-z.

12. Barbie, D.A., Tamayo, P., Boehm, J.S., Kim, S.Y., Moody, S.E., Dunn, I.F., Schinzel, A.C., Sandy, P., Meylan, E., Scholl, C., et al. (2009). Systematic RNA interference reveals that oncogenic KRAS-driven cancers require TBK1. Nature *462*, 108–112. https://doi.org/10.1038/nature08460.

13. Scholl, C., Fröhling, S., Dunn, I.F., Schinzel, A.C., Barbie, D.A., Kim, S.Y., Silver, S.J., Tamayo, P., Wadlow, R.C., Ramaswamy, S., et al. (2009). Synthetic lethal interaction between oncogenic KRAS dependency and STK33 suppression in human cancer cells. Cell *137*, 821–834. https://doi.org/10.1016/j.cell.2009.03.017.

14. Downward, J. (2015). RAS synthetic lethal screens revisited: still seeking the elusive prize? Clin. Cancer Res. *21*, 1802–1809. https://doi.org/10.1158/1078-0432.CCR-14-2180.

15. Blasco, R.B., Francoz, S., Santamaría, D., Cañamero, M., Dubus, P., Charron, J., Baccarini, M., and Barbacid, M. (2011). c-Raf, but not B-Raf, is essential for development of K-Ras oncogene-driven non-small cell lung carcinoma. Cancer Cell *19*, 652–663. https://doi.org/10.1016/j.ccr.2011.04.002.

16. Corcoran, R.B., Cheng, K.A., Hata, A.N., Faber, A.C., Ebi, H., Coffee, E.M., Greninger, P., Brown, R.D., Godfrey, J.T., Cohoon, T.J., et al. (2013). Synthetic lethal interaction of combined BCL-XL and MEK inhibition promotes tumor regressions in KRAS mutant cancer models. Cancer Cell *23*, 121–128. https://doi.org/10.1016/j.ccr.2012.11.007.

17. Verissimo, C.S., Overmeer, R.M., Ponsioen, B., Drost, J., Mertens, S., Verlaan-Klink, I., Gerwen, B.V., van der Ven, M., Wetering, M.v.d., Egan, D.A., et al. (2016). Targeting mutant RAS in patient-derived colorectal cancer organoids by combinatorial drug screening. Elife *5*, e18489. https://doi.org/10.7554/eLife.18489.

18. Wilson, W.H., O'Connor, O.A., Czuczman, M.S., LaCasce, A.S., Gerecitano, J.F., Leonard, J.P., Tulpule, A., Dunleavy, K., Xiong, H., Chiu, Y.L., et al. (2010). Navitoclax, a targeted high-affinity inhibitor of BCL-2, in lymphoid malignancies: a phase 1 dose-escalation study of safety, pharmacokinetics, pharmacodynamics, and antitumour activity. Lancet Oncol. *11*, 1149–1159. https://doi.org/10.1016/S1470-2045(10)70261-8.

19. Corcoran, R.B., Do, K.T., Cleary, J.M., Parikh, A.R., Yeku, O.O., Weekes, C.D., Veneris, J., Ahronian, L.G., Mauri, G., Van Seventer, E.E., et al. (2019). 447PD - phase I/II study of combined BCL-XL and MEK inhibition with navitoclax (N) and trametinib (T) in KRAS or NRAS mutant advanced solid tumours. Ann. Oncol. *30*, v164. https://doi.org/10.1093/annonc/mdz244.009.

20. Fujii, M., Shimokawa, M., Date, S., Takano, A., Matano, M., Nanki, K., Ohta, Y., Toshimitsu, K., Nakazato, Y., Kawasaki, K., et al. (2016). A colorectal tumor organoid library demonstrates progressive loss of niche factor requirements during tumorigenesis. Cell Stem Cell *18*, 827–838. https://doi.org/10.1016/j.stem.2016.04.003.

21. van de Wetering, M., Francies, H.E., Francis, J.M., Bounova, G., Iorio, F., Pronk, A., van Houdt, W., van Gorp, J., Taylor-Weiner, A., Kester, L., et al. (2015). Prospective derivation of a living organoid biobank of colorectal cancer patients. Cell *161*, 933–945. https://doi.org/10.1016/j.cell.2015.03.053.

22. Vlachogiannis, G., Hedayat, S., Vatsiou, A., Jamin, Y., Fernández-Mateos, J., Khan, K., Lampis, A., Eason, K., Huntingford, I., Burke, R., et al. (2018). Patient-derived organoids model treatment response of metastatic gastrointestinal cancers. Science *359*, 920–926. https://doi.org/10.1126/science.aao2774.

23. Ganesh, K., Wu, C., O'Rourke, K.P., Szeglin, B.C., Zheng, Y., Sauvé, C.E.G., Adileh, M., Wasserman, I., Marco, M.R., Kim, A.S., et al. (2019). A rectal cancer organoid platform to study individual responses to chemoradiation. Nat. Med. *25*, 1607–1614. https://doi.org/10.1038/s41591-019-0584-2.

24. Yao, Y., Xu, X., Yang, L., Zhu, J., Wan, J., Shen, L., Xia, F., Fu, G., Deng, Y., Pan, M., et al. (2020). Patient-derived organoids predict chemoradiation responses of locally advanced rectal cancer. Cell Stem Cell *26*, 17–26.e6. https://doi.org/10.1016/j.stem.2019.10.010.

25. Wensink, G.E., Elias, S.G., Mullenders, J., Koopman, M., Boj, S.F., Kranenburg, O.W., and Roodhart, J.M.L. (2021). Patient-derived organoids as a predictive biomarker for treatment response in cancer patients. NPJ Precis. Oncol. *5*, 30. https://doi.org/10.1038/s41698-021-00168-1.

26. Lo, Y.H., Karlsson, K., and Kuo, C.J. (2020). Applications of organoids for cancer biology and precision medicine. Nat. Cancer *1*, 761–773.

27. Pauli, C., Hopkins, B.D., Prandi, D., Shaw, R., Fedrizzi, T., Sboner, A., Sailer, V., Augello, M., Puca, L., Rosati, R., et al. (2017). Personalized in vitro and in vivo cancer models to guide precision medicine. Cancer Discov. *7*, 462–477. https://doi.org/10.1158/2159-8290.CD-16-1154.

28. Ooft, S.N., Weeber, F., Dijkstra, K.K., McLean, C.M., Kaing, S., van Werkhoven, E., Schipper, L., Hoes, L., Vis, D.J., van de Haar, J., et al. (2019). Patient-derived organoids can predict response to chemotherapy in metastatic colorectal cancer patients. Sci. Transl. Med. *11*, eaay2574. https://doi.org/10.1126/scitranslmed.aay2574.

29. Betge, J., Rindtorff, N., Sauer, J., Rauscher, B., Dingert, C., Gaitantzi, H., Herweck, F., Miersch, T., Valentini, E., Hauber, V., et al. (2019). Multiparametric phenotyping of compound effects on patient derived organoids. Preprint at bioRxiv. https://doi.org/10.1101/660993.

30. Lukonin, I., Serra, D., Challet Meylan, L., Volkmann, K., Baaten, J., Zhao, R., Meeusen, S., Colman, K., Maurer, F., Stadler, M.B., et al. (2020). Phenotypic landscape of intestinal organoid regeneration. Nature *586*, 275–280. https://doi.org/10.1038/s41586-020-2776-9.

31. Herpers, B., Eppink, B., James, M.I., Cortina, C., Cañellas-Socias, A., Boj, S.F., Hernando-Momblona, X., Glodzik, D., Roovers, R.C., van de Wetering, M., et al. (2022). Functional patient-derived organoid screenings identify MCLA-158 as a therapeutic EGFR x LGR5 bispecific antibody with efficacy in epithelial tumors. Nat. Cancer *3*, 418–436. https://doi.org/10.1038/s43018-022-00359-0.

32. Jabs, J., Zickgraf, F.M., Park, J., Wagner, S., Jiang, X., Jechow, K., Kleinheinz, K., Toprak, U.H., Schneider, M.A., Meister, M., et al. (2017). Screening drug effects in patient-derived cancer cells links organoid responses to genome alterations. Mol. Syst. Biol. *13*, 955. https://doi.org/10.15252/msb.20177697.

33. Borten, M.A., Bajikar, S.S., Sasaki, N., Clevers, H., and Janes, K.A. (2018). Automated brightfield morphometry of 3D organoid populations by OrganoSeg. Sci. Rep. *8*, 5319. https://doi.org/10.1038/s41598-017-18815-8.

34. Jost, M., Chen, Y., Gilbert, L.A., Horlbeck, M.A., Krenning, L., Menchon, G., Rai, A., Cho, M.Y., Stern, J.J., Prota, A.E., et al. (2017). Combined CRISPRi/a-based chemical genetic screens reveal that Rigosertib is a microtubule-destabilizing agent. Mol. Cell *68*, 210–223.e6. https://doi.org/10.1016/j.molcel.2017.09.012.

35. Jost, M., Chen, Y., Gilbert, L.A., Horlbeck, M.A., Krenning, L., Menchon, G., Rai, A., Cho, M.Y., Stern, J.J., Prota, A.E., et al. (2020). Pharmaceutical-grade Rigosertib is a microtubule-destabilizing agent. Mol. Cell *79*, 191–198.e3. https://doi.org/10.1016/j.molcel.2020.06.008.

36. Moretto, R., Cremolini, C., Rossini, D., Pietrantonio, F., Battaglin, F., Mennitto, A., Bergamo, F., Loupakis, F., Marmorino, F., Berenato, R., et al. (2016). Location of primary tumor and benefit from anti-epidermal growth factor receptor monoclonal antibodies in patients with RAS and BRAF wild-type metastatic colorectal cancer. Oncologist *21*, 988–994. https://doi.org/10.1634/theoncologist.2016-0084.

37. Gregory, R.K., and Smith, I.E. (2000). Vinorelbine–a clinical review. Br. J. Cancer *82*, 1907–1913. https://doi.org/10.1054/bjoc.2000.1203.

38. Marty, M., Fumoleau, P., Adenis, A., Rousseau, Y., Merrouche, Y., Robinet, G., Senac, I., and Puozzo, C. (2001). Oral vinorelbine pharmacokinetics and absolute bioavailability study in patients with solid tumors. Ann. Oncol. *12*, 1643–1649. https://doi.org/10.1023/a:1013180903805.

39. Ogden, A., Rida, P.C.G., Reid, M.D., and Aneja, R. (2014). Interphase microtubules: chief casualties in the war on cancer? Drug Discov. Today *19*, 824–829. https://doi.org/10.1016/j.drudis.2013.10.022.

40. Bajar, B.T., Lam, A.J., Badiee, R.K., Oh, Y.H., Chu, J., Zhou, X.X., Kim, N., Kim, B.B., Chung, M., Yablonovitch, A.L., et al. (2016). Fluorescent indicators for simultaneous reporting of all four cell cycle phases. Nat. Methods *13*, 993–996. https://doi.org/10.1038/nmeth.4045.

41. Kawabata, T., Tanimura, S., Asai, K., Kawasaki, R., Matsumaru, Y., and Kohno, M. (2012). Up-regulation of pro-apoptotic protein Bim and down-regulation of anti-apoptotic protein Mcl-1 cooperatively mediate enhanced tumor cell death induced by the combination of ERK kinase (MEK) inhibitor and microtubule inhibitor. J. Biol. Chem. *287*, 10289–10300. https://doi.org/10.1074/jbc.M111.319426.

42. Wertz, I.E., Kusam, S., Lam, C., Okamoto, T., Sandoval, W., Anderson, D.J., Helgason, E., Ernst, J.A., Eby, M., Liu, J., et al. (2011). Sensitivity to antitubulin chemotherapeutics is regulated by MCL1 and FBW7. Nature *471*, 110–114. https://doi.org/10.1038/nature09779.

43. Jang, W.Y., Lee, J.Y., Lee, S.T., Jun, D.Y., and Kim, Y.H. (2014). Inhibition of JNK2 and JNK3 by JNK inhibitor IX induces prometaphase arrest-dependent apoptotic cell death in human Jurkat T cells. Biochem. Biophys. Res. Commun. *452*, 845–851. https://doi.org/10.1016/j.bbrc.2014.09.015.

44. Waraky, A., Akopyan, K., Parrow, V., Strömberg, T., Axelson, M., Abrahmsén, L., Lindqvist, A., Larsson, O., and Aleem, E. (2014). Picropodophyllin causes mitotic arrest and catastrophe by depolymerizing microtubules via insulin-like growth factor-1 receptor-independent mechanism. Oncotarget *5*, 8379–8392. https://doi.org/10.18632/oncotarget.2292.

45. Brachmann, S.M., Kleylein-Sohn, J., Gaulis, S., Kauffmann, A., Blommers, M.J.J., Kazic-Legueux, M., Laborde, L., Hattenberger, M., Stauffer, F., Vaxelaire, J., et al. (2012). Characterization of the mechanism of action of the pan class I PI3K inhibitor NVP-BKM120 across a broad range of concentrations. Mol. Cancer Ther. *11*, 1747–1757. https://doi.org/10.1158/1535-7163.MCT-11-1021.

46. Komlodi-Pasztor, E., Sackett, D., Wilkerson, J., and Fojo, T. (2011). Mitosis is not a key target of microtubule agents in patient tumors. Nat. Rev. Clin. Oncol. *8*, 244–250. https://doi.org/10.1038/nrclinonc.2010.228.

47. Shi, J., and Mitchison, T.J. (2017). Cell death response to anti-mitotic drug treatment in cell culture, mouse tumor model and the clinic. Endocr. Relat. Cancer *24*, T83–T96. https://doi.org/10.1530/ERC-17-0003.

48. Bennett, A., Sloss, O., Topham, C., Nelson, L., Tighe, A., and Taylor, S.S. (2016). Inhibition of Bcl-xL sensitizes cells to mitotic blockers, but not mitotic drivers. Open Biol. *6*, 160134. https://doi.org/10.1098/rsob.160134.

49. Haschka, M.D., Soratroi, C., Kirschnek, S., Häcker, G., Hilbe, R., Geley, S., Villunger, A., and Fava, L.L. (2015). The NOXA-MCL1-BIM axis defines lifespan on extended mitotic arrest. Nat. Commun. *6*, 6891. https://doi.org/10.1038/ncomms7891.

50. Shi, J., Zhou, Y., Huang, H.C., and Mitchison, T.J. (2011). Navitoclax (ABT-263) accelerates apoptosis during drug-induced mitotic arrest by antagonizing Bcl-xL. Cancer Res. *71*, 4518–4526. https://doi.org/10.1158/0008-5472.CAN-10-4336.

51. Kothari, A., Hittelman, W.N., and Chambers, T.C. (2016). Cell cycle-dependent mechanisms underlie vincristine-induced death of primary acute lymphoblastic leukemia cells. Cancer Res. *76*, 3553–3561. https://doi.org/10.1158/0008-5472.CAN-15-2104.

52. Delgado, M., Urbaniak, A., and Chambers, T.C. (2019). Contrasting effects of microtubule destabilizers versus stabilizers on induction of death in G1 phase of the cell cycle. Biochem. Pharmacol. *162*, 213–223. https://doi.org/10.1016/j.bcp.2018.12.015.

53. Klotz, D.M., Nelson, S.A., Kroboth, K., Newton, I.P., Radulescu, S., Ridgway, R.A., Sansom, O.J., Appleton, P.L., and Näthke, I.S. (2012). The microtubule poison vinorelbine kills cells independently of mitotic arrest and targets cells lacking the APC tumour suppressor more effectively. J. Cell Sci. *125*, 887–895. https://doi.org/10.1242/jcs.091843.

54. Cremolini, C., Pietrantonio, F., Tomasello, G., Dadduzio, V., Moretto, R., Morano, F., Schirripa, M., Antoniotti, C., Fucà, G., Bergamo, F., et al. (2017). Vinorelbine in BRAF V600E mutated metastatic colorectal cancer: a prospective multicentre phase II clinical study. ESMO Open *2*, e000241. https://doi.org/10.1136/esmoopen-2017-000241.

55. Clark, T.B., Kemeny, N.E., Conti, J.A., Huang, Y., Andre, A.M., and Stockman, J. (1998). Phase II trial of docetaxel (Taxotere) for untreated advanced colorectal carcinoma. Cancer Invest. *16*, 314–318. https://doi.org/10.3109/07357909809084650.

56. Swain, S.M., Miles, D., Kim, S.B., Im, Y.H., Im, S.A., Semiglazov, V., Ciruelos, E., Schneeweiss, A., Loi, S., Monturus, E., et al. (2020). Pertuzumab, trastuzumab, and docetaxel for HER2-positive metastatic breast cancer (CLEOPATRA): end-of-study results from a double-blind, randomised, placebo-controlled, phase 3 study. Lancet Oncol. *21*, 519–530. https://doi.org/10.1016/S1470-2045(19)30863-0.

57. Stravodimou, A., and Voutsadakis, I.A. (2019). A systematic review and meta-analysis of the combination of vinorelbine and lapatinib in patients with Her2-positive metastatic breast cancer. Anticancer Res. *39*, 3295–3301. https://doi.org/10.21873/anticanres.13471.

58. Vickers, A.D., Winfree, K.B., Cuyun Carter, G., Kiiskinen, U., Jen, M.H., Stull, D., Kaye, J.A., and Carbone, D.P. (2019). Relative efficacy of interventions in the treatment of second-line non-small cell lung cancer: a systematic review and network meta-analysis. BMC Cancer *19*, 353. https://doi.org/10.1186/s12885-019-5569-5.

59. Amodio, V., Yaeger, R., Arcella, P., Cancelliere, C., Lamba, S., Lorenzato, A., Arena, S., Montone, M., Mussolin, B., Bian, Y., et al. (2020). EGFR blockade reverts resistance to KRAS(G12C) inhibition in colorectal cancer. Cancer Discov. *10*, 1129–1139. https://doi.org/10.1158/2159-8290.CD-20-0187.

60. Ubink, I., Bolhaqueiro, A.C.F., Elias, S.G., Raats, D.A.E., Constantinides, A., Peters, N.A., Wassenaar, E.C.E., de Hingh, I.H.J.T., Rovers, K.P., van Grevenstein, W.M.U., et al. (2019). Organoids from colorectal peritoneal metastases as a platform for improving hyperthermic intraperitoneal chemotherapy. Br. J. Surg. *106*, 1404–1414. https://doi.org/10.1002/bjs.11206.

61. Maurer, U., Charvet, C., Wagman, A.S., Dejardin, E., and Green, D.R. (2006). Glycogen synthase kinase-3 regulates mitochondrial outer membrane permeabilization and apoptosis by destabilization of MCL-1. Mol. Cell *21*, 749–760. https://doi.org/10.1016/j.molcel.2006.02.009.

62. Chao, D.T., Linette, G.P., Boise, L.H., White, L.S., Thompson, C.B., and Korsmeyer, S.J. (1995). Bcl-X(L) and Bcl-2 repress a common pathway of cell-death. J. Exp. Med. *182*, 821–828. https://doi.org/10.1084/jem.182.3.821.

63. Bankhead, P., Loughrey, M.B., Fernández, J.A., Dombrowski, Y., Mcart, D.G., Dunne, P.D., McQuaid, S., Gray, R.T., Murray, L.J., Coleman, H.G., et al. (2017). QuPath: Open source software for digital pathology image analysis. Sci. Rep. *7*, 16878. https://doi.org/10.1038/s41598-017-17204-5.

64. Di Veroli, G.Y., Fornari, C., Wang, D., Mollard, S., Bramhall, J.L., Richards, F.M., and Jodrell, D.I. (2016). Combenefit: an interactive platform for the analysis and visualization of drug combinations. Bioinformatics *32*, 2866–2868. https://doi.org/10.1093/bioinformatics/btw230.

65. Bollen, Y., Hageman, J.H., van Leenen, P., Derks, L.L.M., Ponsioen, B., Buissant des Amorie, J.R., Verlaan-Klink, I., van den Bos, M., Terstappen, L.W.M.M., van Boxtel, R., and Snippert, H.J.G. (2022). Efficient and error-free fluorescent gene tagging in human organoids without double-strand DNA cleavage. PLoS Biol. *20*, e3001527. https://doi.org/10.1371/journal.pbio.3001527.

STAR★METHODS

KEY RESOURCES TABLE

REAGENT or RESOURCE	SOURCE	IDENTIFIER
Antibodies		
Rabbit monoclonal anti-p44/42 MAPK (Erk1/2) (137F5)	Cell Signaling Technology	Cat# 4695; RRID:AB_390779
Rabbit monoclonal anti-phospho-p44/42 MAP kinase (phosphorylated Erk1/2)	Cell Signaling Technology	Cat# 9101; RRID:AB_331646
Rabbit polyclonal anti-Bim	Cell Signaling Technology	Cat# 2819; RRID:AB_10692515
Rabbit monoclonal anti-cleaved PARP (Asp214) (D64E10)	Cell Signaling Technology	Cat# 5625; RRID:AB_10699459
Rabbit monoclonal anti-Mcl-1 (D35A5)	Cell Signaling Technology	Cat# 5453; RRID:AB_10694494
Rabbit monoclonal anti-Bcl-xL (54H6)	Cell Signaling Technology	Cat# 2764; RRID:AB_2228008
Rabbit polyclonal anti-cleaved Caspase-3 (Asp175), for Western Blotting	Cell Signaling Technology	Cat# 9661; RRID:AB_2341188
Rabbit monoclonal anti-cleaved Caspase-3 (Asp175) (D3E9), for IHC staining	Cell Signaling Technology	Cat# 9579; RRID:AB_10897512
Rabbit polyclonal anti-phospho-EGF Receptor (Tyr1068)	Cell Signaling Technology	Cat# 2234; RRID:AB_331701
Rabbit monoclonal anti-EGF Receptor (D38B1)	Cell Signaling Technology	Cat# 4267; RRID:AB_2246311
Mouse monoclonal anti-Vinculin (Clone hVIN-1)	Sigma-Aldrich	Cat# V9131; RRID:AB_477629
Mouse monoclonal anti-human-Cytokeratin (Clone CAM5.2)	BD Biosciences	Cat# 345779; RRID:AB_2800363
Mouse monoclonal anti-human-Ki67 (Clone MM1)	Cell Sciences	Cat# MONX10283; RRID:AB_1833494
Rat monoclonal anti-alpha-Tubulin (YL1/2)	Santa Cruz Biotechnology	Cat# sc-53029; RRID:AB_793541
Goat polyclonal anti-Rat IgG (H + L) Cross-Adsorbed Secondary Antibody, Alexa Fluor 568	Thermo Fisher Scientific	Cat# A-11077; RRID:AB_2534121
Mouse monoclonal anti-β-Actin (Clone AC-74)	Sigma-Aldrich	Cat# A2228; RRID:AB_476697
Biological samples		
Colorectal Cancer (CRC) Patient-derived organoid (PDO) line P6T	van de Wetering et al.[21]	I2L-P6-Tumor-Organoid; techtransfer@huborganoids.nl
CRC PDO line P9T	van de Wetering et al.[21]	I2L-P9-Tumor-Organoid; techtransfer@huborganoids.nl
CRC PDO line P16T	van de Wetering et al.[21]	I2L-P16-Tumor-Organoid; techtransfer@huborganoids.nl
CRC PDO line P19bT	van de Wetering et al.[21]	I2L-P19bT-Tumor-Organoid; techtransfer@huborganoids.nl
CRC PDO line P24aT	van de Wetering et al.[21]	I2L-P24a-Tumor-Organoid; techtransfer@huborganoids.nl
CRC PDO line P26T	van de Wetering et al.[21]	I2L-P26-Tumor-Organoid; techtransfer@huborganoids.nl
CRC PDO line P18T-KRAS	Verissimo et al.[17]	N/A
CRC PDO line B2-002	Hubrecht Organoid Technology; www.huborganoids.nl	HUB-02-B2-002; techtransfer@huborganoids.nl
CRC PDO line B2-006	Hubrecht Organoid Technology; www.huborganoids.nl	HUB-02-B2-006; techtransfer@huborganoids.nl
CRC PDO line B2-025	Hubrecht Organoid Technology; www.huborganoids.nl	HUB-02-B2-025; techtransfer@huborganoids.nl
CRC PDO line B2-040	Hubrecht Organoid Technology; www.huborganoids.nl	HUB-02-B2-040; techtransfer@huborganoids.nl

(*Continued on next page*)

Continued

REAGENT or RESOURCE	SOURCE	IDENTIFIER
CRC PDO line B2-047	Hubrecht Organoid Technology; www.huborganoids.nl	HUB-02-B2-047; techtransfer@huborganoids.nl
CRC PDO line B2-054	Hubrecht Organoid Technology; www.huborganoids.nl	HUB-02-B2-054; techtransfer@huborganoids.nl
CRC PDO line B2-055	Hubrecht Organoid Technology; www.huborganoids.nl	HUB-02-B2-055; techtransfer@huborganoids.nl
CRC PDO line C2-055	Hubrecht Organoid Technology; www.huborganoids.nl	HUB-02-C2-055; techtransfer@huborganoids.nl
CRC PDO line B2-060	Hubrecht Organoid Technology; www.huborganoids.nl	HUB-02-B2-060; techtransfer@huborganoids.nl
CRC PDO line B2-070	Hubrecht Organoid Technology; www.huborganoids.nl	HUB-02-B2-070; techtransfer@huborganoids.nl
CRC PDO line B2-071	Hubrecht Organoid Technology; www.huborganoids.nl	HUB-02-B2-071; techtransfer@huborganoids.nl
CRC PDO line B2-074	Hubrecht Organoid Technology; www.huborganoids.nl	HUB-02-B2-074; techtransfer@huborganoids.nl
CRC PDO line B2-084	Hubrecht Organoid Technology; www.huborganoids.nl	HUB-02-B2-084; techtransfer@huborganoids.nl
CRC PDO line B2-092	Hubrecht Organoid Technology; www.huborganoids.nl	HUB-02-B2-092; techtransfer@huborganoids.nl
CRC PDO line B2-096	Hubrecht Organoid Technology; www.huborganoids.nl	HUB-02-B2-096; techtransfer@huborganoids.nl
CRC PDO line B2-113	Hubrecht Organoid Technology; www.huborganoids.nl	HUB-02-B2-113; techtransfer@huborganoids.nl
CRC PDO line B2-123	Hubrecht Organoid Technology; www.huborganoids.nl	HUB-02-B2-123; techtransfer@huborganoids.nl
CRC PDO line B2-130	Hubrecht Organoid Technology; www.huborganoids.nl	HUB-02-B2-130; techtransfer@huborganoids.nl
CRC PDO line B2-153	Hubrecht Organoid Technology; www.huborganoids.nl	HUB-02-B2-153; techtransfer@huborganoids.nl
CRC PDO line C2-153	Hubrecht Organoid Technology; www.huborganoids.nl	HUB-02-C2-153; techtransfer@huborganoids.nl
Pancreatic PDO line PANC1	Hubrecht Organoid Technology; www.huborganoids.nl	HUB-08-B2-013A; techtransfer@huborganoids.nl
Pancreatic PDO line PANC2	Hubrecht Organoid Technology; www.huborganoids.nl	HUB-08-B2-019A; techtransfer@huborganoids.nl
Pancreatic PDO line PANC3	Hubrecht Organoid Technology; www.huborganoids.nl	HUB-08-B2-024B; techtransfer@huborganoids.nl
Pancreatic PDO line PANC4	Hubrecht Organoid Technology; www.huborganoids.nl	HUB-08-B2-053B; techtransfer@huborganoids.nl
Pancreatic PDO line PANC5	Hubrecht Organoid Technology; www.huborganoids.nl	HUB-08-B2-026A; techtransfer@huborganoids.nl
Pancreatic PDO line PANC6	Hubrecht Organoid Technology; www.huborganoids.nl	HUB-08-B2-027A; techtransfer@huborganoids.nl
Non-small Cell Lung Cancer (NSCLC) PDO line	Hubrecht Organoid Technology; www.huborganoids.nl	HUB-07-B2-047; techtransfer@huborganoids.nl
CRC PDO line TOR14	Ubink et al.[60]	TOR14; techtransfer@huborganoids.nl
CRC PDO line TOR20	Ubink et al.[60]	TOR20; techtransfer@huborganoids.nl
CRC PDO line TOR22	Ubink et al.[60]	TOR22; techtransfer@huborganoids.nl
Chemicals, peptides, and recombinant proteins		
Advanced DMEM/F12	ThermoFisher Scientific	Cat# 12634010

(*Continued on next page*)

Continued

REAGENT or RESOURCE	SOURCE	IDENTIFIER
B27 supplement	ThermoFisher Scientific	Cat# 17504044
RhoKinase inhibitor Y-27632	Gentaur	Cat# A3008
N-Acetyl-L-Cysteine	Sigma-Aldrich	Cat# A9165
Nicotinamide	Sigma-Aldrich	Cat# N0636
A83-10	Tocris	Cat# 2939/10
SB202190	Gentaur	Cat# A1632
EGF (Recombinant Human EGF)	PeproTech	Cat# AF-100-15
GlutaMAX	ThermoFisher Scientific	Cat# 35050-038
HEPES	ThermoFisher Scientific	Cat# 15630-056
Penicillin/Streptomycin	Lonza	Cat# DE17-602E
Matrigel	Corning	Cat# 356231
Basement membrane extract (BME)		N/A
Dispase II	ThermoFisher Scientific	Cat# 17105041
Trypsin EDTA	Sigma-Aldrich	Cat# 25200056
Trypsin Inhibitor from Soybean	Sigma-Aldrich	Cat# T9003
Puromycin	Sigma-Aldrich	Cat# P7255
Primocin	InvivoGen	Cat# ant-pm-1
Hoechst 33342	ThermoFisher Scientific	Cat# 62249
Propidium Iodide	ThermoFisher Scientific	Cat# P3566
SYTOX™ Green	ThermoFisher Scientific	Cat# S7020
Anti-cancer compound library (414 cpds)	Selleck Chemicals	L3000
Binimetinib (MEK162)	Selleck Chemicals	Cat# S7007
Vinblastine (NSC-49842) sulfate	Selleck Chemicals	Cat# S4505
SU6656	Selleck Chemicals	Cat# S7774
Venetoclax (ABT-199)	Selleck Chemicals	Cat# S8048
S63845	Selleck Chemicals	Cat# S8383
Fluorouracil (5-Fluorouracil, 5-FU)	Selleck Chemicals	Cat# S1209
SN-38	Selleck Chemicals	Cat# S4908
Oxaliplatin (NSC 266046)	Selleck Chemicals	Cat# S1224
Z-VAD-FMK	Selleck Chemicals	Cat# S7023
WEHI-539 hydrochloride	MedChemExpress	HY-15607A
Staurosporine	Sigma-Aldrich	Cat# S6942
Critical commercial assays		
AlamarBlue™ Cell Viability Reagent	ThermoFisher Scientific	Cat# DAL1100
CellTox™ Green Cytotoxicity Assay	Promega	Cat# G8731
Click-iT™ EdU Alexa Fluor™ 488 Flow Cytometry Kit	ThermoFisher Scientific	Cat# C10425
CellEvent™ Caspase-3/7 Detection Reagent	ThermoFisher Scientific	Cat# C10723
Deposited data		
Primary screening data CRC PDO P9T	This paper	Table S2
Experimental models: Cell lines		
HA-RSpondin1-Fc 293T cell line to make R-Spondin CM	In-house production	N/A
HEK293-mNoggin-Fc cell line to make Noggin CM	In-house production	N/A
Experimental models: Organisms/strains		
Mouse: NOD.Cg-*Prkdc*^{scid} *Il2rg*^{tm1Wjl}/SzJ	The Jackson Laboratory	JAX: 005557
Oligonucleotides		
See Table S4	This paper	N/A

(*Continued on next page*)

Continued

REAGENT or RESOURCE	SOURCE	IDENTIFIER
Recombinant DNA		
pInd-TRE-mKate2-NLS-P2A-MCL1	This paper	N/A
pInd-TRE-mKate2-NLS-P2A-BCL-xL	This paper	N/A
pTOPO-MCL1	Maurer et al.[61]	Addgene Plasmid #21605
pSFFV-neo BCL-xL	Chao et al.[62]	Addgene Plasmid # 8749
pLV-H2B-mScarlet-I-Ires-Puro	This paper	N/A
pLL3.7m-Clover-Geminin(1–110)-IRES-mKO2-Cdt(30–120)	Bajar et al.[40]	Addgene Plasmid #83841
pLL3.7m-mTurquoise2-SLBP(18–126)-IRES-H1-mMaroon1	Bajar et al.[40]	Addgene Plasmid #83842
Software and algorithms		
GraphPad Prism v9.5.1	GraphPad software	https://www.graphpad.com/
ImageJ v1.53c	NIH	https://imagej.nih.gov/ij/
QuPath v0.3.2	Bankhead et al.[63]	https://qupath.github.io/
ImageJ macro to Measure fluorescent intensities (Fucci4) in max-projected 3D-images	This paper	Zenodo database: https://zenodo.org/badge/latestdoi/611264281
Imaris Viewer software	Oxford Instruments	https://imaris.oxinst.com/imaris-viewer
Combenefit	Di Veroli et al.[64]	https://sourceforge.net/projects/combenefit/
Columbus Image data storage and analysis system v2.7	Perkin Elmer	https://www.perkinelmer.com/product/image-data-storage-and-analysis-system-columbus

RESOURCE AVAILABILITY

Lead contact

Further information and requests for resources and reagents should be directed to and will be fulfilled by the lead contact, Hugo J.G. Snippert (h.j.g.snippert@umcutrecht.nl).

Materials availability

Patient-derived organoids identified by the HUB codes HUB-02-B2-xxx, P-6/9/16/18/19b/24a/26-T, TOR14/20/22 (all from CRC), pancreatic cancer (PANC1-6) and non-small cell lung cancer (NSCLC) organoids are cataloged at www.huborganoids.nl and can be requested at techtransfer@huborganoids.nl. Distribution to third (academic or commercial) parties will have to be authorised by the Biobank Research Ethics Committee of the University Medical Center Utrecht (TCBio) at request of Hubrecht Organoid Technology (HUB). CRC PDO P18T-KRAS is available from the lead contact with a completed Materials Transfer Agreement.

Data and code availability

- All raw data reported in this paper will be shared by the lead contact upon request.
- The custom FIJI code used in this study for the parallel measurement of multichannel fluorescent intensities is available at Zenodo database: https://zenodo.org/badge/latestdoi/611264281.
- Any additional information required to reanalyze the data reported in this paper is available from the lead contact upon request.

EXPERIMENTAL MODEL AND SUBJECT DETAILS

Animals

Mice experiments were conducted at the Mouse Cancer Clinic (Netherlands Cancer Institute). Approval for these studies was obtained by the local animal experimental committee (DEC-NKI; AVD = 301002016407, EGP 8926, EGP 8401 and EGP 9104). Eight-12 weeks old NOD.Cg-*Prkdc*^{scid} *Il2rg*^{tm1Wjl}/SzJ (NOD-Scid) mice (JAX stock no: 005557) were used for subcutaneous injections with PDO P9T organoids, as well as for pharmacokinetic analysis Mice were randomly stratified into experimental groups, maintaining a 50% female 50% male distribution.

Patient-derived organoid (PDO) culture and maintenance

The collection of patient tissue for the generation and distribution of organoids has been performed according to the guidelines of the European Network of Research Ethics Committees (EUREC) following European, national, and local law. In all cases, patients signed informed consent after ethical committees approved the study protocols.

CRC patient-derived organoids with identifiers P-6/9/16/18/19b/24a/26-T and TOR14/20/22 were previously established and characterized.[21,60] These and all other PDOs used in this study are cataloged and can be requested at www.huborganoids.nl. We refer to the key resource table and Table S3 for extensive description of patient derived organoid lines nomenclature, catalog numbers and recurrent cancer mutations. CRC PDO P18T-KRAS has been generated through CRISPR-mediated introduction of the $KRAS^{G12D}$ mutation in PDO P18T and has been described previously.[17]

Organoid identity was verified through genotyping of unique combinations of driver mutations by PCR on gDNA. using primers amplifying TP53 with primer set 1: FW (ACAACCAGGAGCCATTGTCTT) and RV (CCTCCCCTGCTTGCCAC) and primer set 2: FW (CTGTGCAATAGTTAAACCCATTT) and RV (CAGCAGCTCCTACACCG), KRAS with FW (CCGCAGAACAGCAGTCTG) and RV (TGAT GTCACAATACCAAG) and sequence primer (CACCGATACACGTCTGCAGTCAAC), NRAS with FW (GCAATTTGAGGGACAA ACC) and RV (CCTCTCTGAAATTCCTTCG) and sequence primer (GTCATTCCCAGTAGCAAG) and BRAF with FW (CTTCATAATG CTTGCTCTG) and RV (GCCTCAATTCTTACCATC) and sequence primer (CCTGCCTTAAATTGCATAC).

CRC PDOs were cultured as described previously.[21] In short, organoids were cultured in drops of Basement Membrane Extract (BME; Amsbio) or Matrigel (MG; Corning) and medium was refreshed every two days. The CRC culture medium contained advanced DMEM/F12 (Invitrogen) with 1% Penicillin/Streptomycin (P/S, Lonza), 1% HEPES buffer (Invitrogen) and 1% Glutamax (Invitrogen), 20% R-spondin conditioned medium, 10% Noggin conditioned medium, 1X B27 (Invitrogen), 1.25 mM n-Acetyl Cysteine (Sigma-Aldrich), 10 mM Nicotinamide (Sigma-Aldrich), 50 ng/mL EGF (Peprotech), 500 nM A83-01 (Tocris), 10 mM SB202190 (Gentaur). Organoids were splitted through shear stress (pipetting) and/or Trypsin-EDTA (Sigma-Aldrich) treatment. Trypsin activity was abrogated using 0.5 mg/mL soybean trypsin inhibitor (Sigma-Aldrich). Residual trypsin was washed out using Advanced DMEM/F12, the cells were resuspended in MG/BME, and cultured for the first two days with 10 μM Y-27632 dihydrochloride (Gentaur) for maintenance.

METHOD DETAILS

Drug library, targeted inhibitors and additional reagents

The anti-cancer compound library (414 compounds, #L3000) and the individual compounds Binimetinib (MEK162), Vinblastine sulfate, SU6656, Venetoclax (ABT-199), S63845, 5-Fluorouracil, Oxaliplatin (NSC 266046), SN-38 and Z-VAD-FMK were all purchased from Selleckchem, WEHI-539 hydrochloride from MedChemExpress and Staurosporine from Sigma-Aldrich.

Immunofluorescence stainings

For live/death cell stainings organoid cultures were incubated with 10 μg/mL Propidium Iodide (PI) and 10 μg/mL Hoechst33342 (both from ThermoScientific) for 30 min at 37°C. Organoids were washed 3 times 10 min with CRC medium to remove unbound label and then fixed *in situ* with 1% paraformaldehyde (PFA, VWR) and 0.5% Glutaraldehyde (Sigma-Aldrich) for 20 min at room temperature (RT) and then stored in D-PBS (ThermoFisher) at 4°C until image acquisition. For α-Tubulin stainings, organoid cultures were washed with D-PBS and fixed *in situ* with 1% PFA/0.5% Glutaraldehyde. Subsequently, organoids were washed with D-PBS and free aldehydes were quenched by washing with 1% sodium borohydride (Sigma- Aldrich) at RT 3 times 10 min. Upon washing with D-PBS, organoids were permeabilized and blocked at 4°C in PBD2T buffer (1% BSA, 10%DMSO, 2% Triton X-100 (VWR) in D-PBS). Fixed organoids were stained with primary and secondary antibodies overnight in PBD2T, washed extensively with D-PBS and then stored in D-PBS containing 10 μg/mL Hoechst33342 at 4°C until image acquisition with either Zeiss LSM510 or LSM880 confocal microscopy systems. Image processing was performed with ImageJ/Fiji. Antibodies used were α-Tubulin (YL1/2) (RRID:AB_793541)and goat anti-rat IgG (H + L) Alexa Fluor 568 (ThermoFisher).

Drug screening on PDO cultures

Five-to-seven day (after seeding) organoid cultures were dislodged from BME using 1 mg/mL dispase II (ThermoFisher) for 15 min at 37°C. Subsequently, organoids were mechanically dissociated by pipetting, filtrated using a 70μm nylon cell strainer (Falcon) and resuspended in CRC medium containing 2% BME. Organoids were plated (Multi-drop Combi Reagent Dispenser) at a density of ~500/well on BME pre-coated 384-well plates (Greiner). The drugs and their combinations were added 3hrs after plating the organoids using a Tecan D300e Digital Dispenser prior to sealing the plates with Breathe-easy membranes (Sigma-Aldrich). Drug plates were normalized with vehicle (DMSO) to a maximum concentration of 0.5%. Standardly, 72hrs after adding the drugs, organoids were fixed overnight using 1% PFA and 0.5% Glutaraldehyde (Sigma-Aldrich) in the presence of 10 μg/mL Hoechst (final concentrations), prior to image acquisition or were used immediately for metabolic assays. Individual screening plates standardly contained wells consisting of only vehicle, or 20μM Navitoclax, used as negative and positive plate controls, respectively. Where indicated, wells containing a fixed concentration of one of the pan-HER/MEK inhibitor combinations (1μM Afa + 1μM Sel for the primary screen) served as additional negative plate controls. Independent of screening output format, all data were normalized to positive and negative plate controls (in GraphPad Prism 8), prior to further analysis.

For the primary drug screen, library drugs were added in duplicate wells/plate in a 5-step logarithmic concentration range from 5nM to 20μM and on duplicate plates, combined with DMSO or the therapeutic backbone. Plate Z-factors were calculated on raw data as described (Zhang et al., JBiomolScreen, 1999) with Z = S/R, where S=(mean survival$_{\text{negative control}}$ − 3 · SD $_{\text{negative control}}$) - (mean survival$_{\text{positive control}}$ + 3 · SD $_{\text{positive control}}$) and R=(mean survival$_{\text{negative control}}$) - (mean survival$_{\text{positive control}}$), using the above-mentioned. For validation and additional screens, drugs were added in triplicate wells/plate using a ≥7-step logarithmic concentration range from 5nM to 20μM.

Metabolic endpoint assays using AlamarBlue (AB) cell viability reagent (ThermoFisher) were performed as described previously (Verissimo, 2016). Briefly, at the end of the drug screens, organoids were incubated with CRC-medium containing 2%BME and 10% AB for 2 h at 37°C. The change in AB fluorescence (544/590nm, ex/em) was measured on a SpectraMax M5 microplate reader (Molecular Devices). After correction of background fluorescence (RFU at time point 0 of individual wells), cell viability was defined relative to the mean fluorescence of vehicle treated controls.

Due to the dispersed (grape-like) morphology of PDO HUB-B2-96, making it unsuitable to determine an image-based C-score, CellTox Green dye (Promega) was used instead to monitor drug-induced toxicity. Approximately 4000 organoids/well of a 384-well plate were seeded in phenol red free advanced DMEM/F12 (Invitrogen), to optimize signal-to-noise ratio. CellTox Green was added (1000x diluted) at the end of the drug exposure, incubated for 30 min at 37°C, upon which fluorescence was read (ex 510 nm, em ≥ 550 nm) using a SpectraMax M5 microplate reader (Molecular Devices).

Image based analysis of drug toxicity on PDO cultures

Image acquisition of 384-well plates was performed with a CellInsight CX5 High Content Screening (HCS) device (Thermo Scientific), using a 4x microscope objective (Olympus) for whole-well imaging. Organoid morphology was assessed by 2 channel imaging of 3–5 z-planes (spanning ~190-315μm), using transmitted light (for visual inspection of overall morphology) and Hoechst fluorescence (386⁄440nm, ex/em) for software autofocusing and image quantification. Images were processed using the Columbus (version 2.7) image analysis platform (PerkinElmer). Batch object segmentation was performed using "Method A or C" in the analysis pipeline, using z-projected images of the Hoechst channel. Morphologic parameters circularity (C) and size (2D surface area) were generated per segmented object (organoid). Circularity is calculated on a scale of 0–1, with 1 being a perfect circle. C is proportional to the sqrt of the area over the circumference, normalized to give 1.0 for a perfect circle (Columbus, PerkinElmer). Optimal object segmentation settings were defined per plate, using the highest difference in mean circularity between positive and negative control wells as primary variable. To define organoid survival, acquired objects (excluding border objects) were filtered by size; Small ($<1.5 \cdot 10^3$ μm^2) segmented objects (reflecting single cells or dead cell fragments, share a high intrinsic degree of circularity. These objects (and to a minor extent large/fused objects) complicate the discriminative power of the assay and were excluded from further analysis. We noticed limited impact of PDO seeding densities (from 50 to 1250 PDOs/384-well) on C-score assignment, with the exception that the sensitivity of PDOs to targeted drugs like Afa and Sel changed with increasing PDO density (Figure S3C). Drug sensitivity stabilized with seeding densities >500 PDOs/well, making this density the minimal threshold for all experiments.

C-scores were converted to viability scores (in Microsoft Excel) per 384-well plate using a dynamic threshold (range: 0.65-0.9) of the C-score. In brief, for each individual C-score threshold, the percentage of organoids above/below that threshold was determined for pooled data of all negative (DMSO) and positive (20μM Nav) control wells per plate. The optimal threshold was defined by the largest percentage difference between these controls (optimal discrimination between C-score distributions) and was subsequently applied to all segmented objects, to obtain a viability percentage for individual wells within the drug-treated plate (see Figure 1). Viability values of ~250 organoids/well were determined and used to generate dose-response curves. For image based analysis of organoid size, segmented objects were filtered by area (50000μm2 ≥ size ≥ 100μm^2) to exclude artifacts (fused objects) and single cells. Relative organoid size was calculated by normalization to untreated controls (relative size = 1) and organoids treated with 20μM Nav (rel size = 0).

For object based quantification of drug toxicity (Figure 1E) and drug-pulse experiments (Figure 3G), P9T PDOs were seeded (~750/well) on MG filled 96-well angiogenesis culture/imaging plates (IBIDI) to mimic 384-well screening conditions and create a meniscus-free surface to facility imaging and downstream analysis.

Curve fitting of drug sensitivity and multi-comparison analysis

For the primary drug screen, results were normalized to vehicle (DMSO = 100%) or the therapeutic backbone (1μM Afa/Sel = 100%) as negative controls and 20μM Nav (= 0%) as positive control. Then, drug dose-response curves and IC_{50} values were generated by nonlinear regression fitting to a variable slope, normalized three-parameter model. IC_{50} values predicted by this model were excluded if the mean effect of the highest concentration (20μM) of the drug (or its combination), did not clearly deviate from the mean effect of the plate control. As such, we defined that the standard deviations of the mean of the treatment could not overlap with that of the control. ΔIC_{50} was calculated as (IC_{50} monotherapy)/(IC_{50} triplet combination).

For additional screens, dose-response curves were generated by nonlinear regression fitting to a variable slope, LOG(inhibitor) vs. response model, using a top constrain of 100%. AUC values were generated by GraphPad and ΔAUC was calculated as (($AUC_{\text{monotherapy}}$ − $AUC_{\text{triplet combination}}$)/(maximum AUC from control)) · 100%.

To visualize and calculate drug combination effects we used the free software package Combenefit.[64] Screening data were first normalized to vehicle (for the Lap/Bini combination) or 120nM VNRB treatments (for the triplet combination) and 20μM Nav. Synergy scores were calculated using the classical Bliss model.

Multiple comparisons between drug-sensitivity and clinical/genetic tumor features were performed by either two-tailed t-tests (comparing 2 groups) or ordinary one-way ANOVA (>2 groups) and p values plotted as a heatmap. ANOVA post-hoc analysis multi-comparison analysis was performed using Fisher's LSD test. Curve fitting and statistical analysis were performed with Graphpad Prism (v9).

Vector construction and organoid modification

Plasmids pTOPO-MCL1 (Addgene #21605) and pSFFV-neo BCL-xL (Addgene #8749) were used as template to clone full length human MCL1 and BCL-xL into a pInducer20 lentiviral vector variant modified to express mKate2-NLS as a P2A-coupled reporter fluorophore (described in Ponsioen et al., 2021). Briefly, N17Ras was replaced by MCL1 or BCL-xL, fusing their N-terminus to the P2A self-cleaving peptide, using In-Fusion HD Cloning Kit (Clontech Laboratories) with the following PCR-primers (where the P2A sequence and start codons are bold and underlined respectively):

MCL1_FW (CCCTGGACCTGCTAGCATGTTTGGCCTCAAAAGAAACGC) and MCL1_RV (GCCCTCTAGACTCGAGCTATCTTATT AGATATGCCAAACCAGCTCCT) and BCL-xL_FW (CCCTGGACCTGCTAGCATGTCTCAGAGCAACCGGG) and BCL-xL_RV (GCCC TCTAGACTCGAGTCATTTCCGACTGAAGAGTGAGCC).

Constructs were sequence verified prior to use. Lentivirus production and organoid infection were performed as described previously (Oost et al., 2018). Four days after infection of P9T PDOs with mKATE2-P2A-MCL1/BCL-xL inducible vectors, organoids were selected with 2 μg/mL puromycin (Sigma-Aldrich). Upon selection, mKATE2 expression was induced for 8hrs with 1 μg/mL doxycycline (Bio-Connect). Next, organoids were harvested with dispase and trypsinized as described before. Single cells were resuspended in CRC medium containing 100 μg/mL Primocin (InvivoGen) and 10 μM Y-27632 and filtered using a 40 μm strainer (VWR). mKATE2 positive cells were isolated by flow cytometry on an Aria III machine (Becton Dickinson), collected in CRC medium with 100 μg/mL primocin, 10 μM Y-27632 and 2% v/v MG and expanded for further studies.

To generate P9T PDOs stably expressing the FUCCI4 reporter system (Bajar et al., 2016), organoids were co-infected with lentiviral vectors pLL3.7m-Clover-Geminin(1–110)-IRES-mKO2-Cdt(30–120) and pLL3.7m-mTurquoise2-SLBP(18–126)-IRES-H1-mMaroon1 (Addgene, plasmids #83841 and #83842 respectively). Five days after expression, FUCCI4-positive cells were isolated by flow cytometry (as described), selecting mMaroon1 positive cells, which were simultaneously positive for either of the tandemly expressed mKO2 or mClover. To enrich for cells showing long-term stable expression of both reporter constructs, flow-sorting was repeated after 3 weeks of culture. Subsequently, clonal organoid structures were hand-picked, expanded and verified by confocal microscopy (Leica TCS SP8X) for the expression of all 4 reporters.

P6T, P16T and P26T PDOs, used for time-lapse microscopy, were modified by lentiviral transduction (as described) using lentivirus encoding Histone2B fused to mScarlet-I (bright mono-meric red fluorescent protein) linked to a puromycin-resistance gene (pLV-H2B-mScarlet-I-ires-Puro) to visualize and track nuclei. The vector was generated by replacing mNeonGreen (from pLV-H2B-mNeonGreen-ires-Puro, described in[17]) with mScarlet-I, amplified from TV-mScarlet-I (Addgene #169218[65]) with primers mScarlet-I_FW (CTAAGGATCCACCGGTCGCCACCATGGTGAGCAAGGGCG) and mScarlet-I_RV (AATGTTAACGACCGGTTAGCT AGCCTTGTACAGCTCGTCCATGCC), using AgeI-NheI rescriction sites. Infected organoids were selected using 2 μg/mL puromycin.

Object based quantification of drug toxicity, correlating organoid circularity to death cell markers

P6T, P9T and P16T PDOs were grown on 96-well angiogenesis plates (IBIDI) as described. Drug treatments and media formulation were identical to the 384-well plate based screen. For PI incorporation experiments, organoids treated for 72hrs with drugs were stained with PI/Hoechst33342 as described. Organoids were washed 3 times 5 min with advanced DMEM/F12 to remove unbound label and then fixed with 1% PFA/0.5% Glutaraldehyde. Single z-plane confocal images (Zeiss LSM880) of $\geq$15 organoids/condition (encompassing 3–8 individual images) were acquired and used for analysis. Images were smoothened and processed using the 'adaptive threshold' plugin in ImageJ (1.53c, National Institutes of Health). The resulting binary images were used for image segmentation in Columbus (PerkinElmer). Intact and fragmented nuclei were identified and counted for both fluorescent channels, using 'method C' in the 'find nuclei' block of the image analysis pipeline. Mean percentage toxicity was calculated by averaging the ratios (PI-positive objects)/(Hoechst-positive objects) of all images/condition. Subsequently, data were normalized to positive and negative plate controls, prior to dose-response curve fitting (GraphPad Prism9).

To establish a correlation between C-scores and additional cell death markers, PDOs were incubated with Nav in a concentration range (11 steps) from 5nM to 20μM for a total of 72hrs. For the final 6hrs of the experiment the fluorescent nuclear death markers CellEvent Caspase3/7-activity probe (1μM final concentration, ThermoFisher Scientific) or SYTOX-green (5nM final concentration, ThermoFisher Scientific) were added in independent wells. Nuclei were stained with Hoechst33342. Widefield image acquisition of 96-well plates was performed, similar to the screening method, capturing the fluorescent intensities of the used markers on a whole-well level. Images were processed using Columbus (as already described), to establish C-scores and integrated fluorescent intensities per segmented organoid. Caspase/Hoechst and SYTOX/Hoechst intensity ratios were plotted against C-scores, and their correlation (Pearson r-values) were determined in Graphpad Prism 9. The Caspase3/7-activity probe showed reduced fluorescent intensity in wells treated with high doses of Nav, where organoids died early in the experiment and lost Caspase enzymatic activity

at the end of the 72hrs time course. Hence, we used only data up to the IC100 of Nav (based on C-scores and observed morphology) to determine correlations using this probe.

BCL-xL/MCL1 induced rescue of triplet-combination induced organoid death

P9T PDOs stably expressing inducible BCL-xL and MCL1 constructs were seeded on MG filled 96-well angiogenesis plates (IBIDI) as described before. Twenty-four hr before drug treatment, organoids were treated with either 1 μg/mL DOX ('normal' concentration), 0.125 ng/mL DOX ('low' concentration) or left untreated. Parallel cultures were treated similarly for the full duration of the experiment, harvested by dispase and processed to single cells to evaluate mKate2 expression on a BD FACSCelesta flow cytometer. Drug treated 3D cultures were imaged semi-automatically using the CellInsight system as described. For increased accuracy, organoid integrity was quantified manually in ImageJ/Fiji. Survival scores are relative to vehicle treated controls and are mean data of three independent experiments (using duplicate wells/experiment).

Time lapse microscopy and analysis of cell killing in relation to mitosis

For time-lapse imaging of FUCCI4-reporter expressing P9T PDOs, 5-day (from single cell seeding) cultures were plated in MG on segmented glass-bottom dishes (Greiner) and mounted on an inverted confocal microscope equipped with an Argon- and a white light-laser (Leica TCS SP8X) under controlled conditions (37°C, 6% CO2). Drugs were added to the organoids ~3hr prior to imaging and the four tested conditions were recorded simultaneously. During 72hrs, organoids were imaged every 20 min in XYZT-mode using a 40x objective (1.1NA). Z-stacks of only the lower half of the 3D organoids were recorded, to minimize loss of fluorescent signal in the z-dimension and create minimal overlap of individual cells in 2D z-projections. Next, depth-coded z-projected movies (based on mMaroon-Histone1) were analyzed for apoptotic events, i.e. they were manually marked with help of custom-made 'event-viewer' ImageJ macro, as described previously (Verissimo et al., 2016). Marked events were automatically drawn in the movie and data were automatically sorted into Excel-files as a chronological list of events. A custom made ImageJ/Fiji 'Fucci4-readout' macro was used, in which 'event-viewer' movies were simultaneously opened and synchronized with the 4 individual channels of the FUCCI4 reporter (maximum z-projections of the raw recorded signals). Previously marked apoptotic events were used as guide to track these cells 1–2 frames back in time. The macro allows for manual drawing of a ROI, which is automatically copied to the FUCCI4 channels, from which the mean pixel intensities are measured (after background subtraction). ROIs were selected such as to exclude signals from overlapping neighboring nuclei. Measured fluorescence intensities were processed in Excel to generate ratios for each tandem of fluorophores expressed from the same lentiviral vector (see above); ratio 1: mKO2-Cdt/Clover-Geminin, ratio 2: mTurquoise2-SLBP/H1-mMaroon1. To exclude noise, ratios were only included if the mMaroon1 signal (which should always be present) exceeded background by 2-fold. To define valid ratio thresholds for the classification of the different cell cycle phases, >70 mitotic events from vehicle treated organoids were tracked over time. G2 events were defined by backtracking 1–2 frames from mitotic onset, which were clearly recognized by pro-metaphase/metaphase chromosome condensation.

Apoptotic and mitotic events of (5-day old) cultures of Histone2B-mScarletI expressing PDOs P6T, P16T and P26T were recorded every 15 min on a Nikon TiE inverted spinning disc microscope using the described conditions. Apoptotic events (>60 per condition) were scored and tracked back in time to the onset of a potential mitotic event. Manual scoring was performed by 2 objective observers, using the above-mentioned ImageJ macro or free Imaris Viewer software (Oxford Instruments). Mitosis was called aberrant when exceeding the normal time span (>1hr, arrest), when incomplete (slippage), or leading to >2 daughter nuclei. Dot-plots and pie-diagrams were generated in GraphPad Prism 9.

Double thymidine experiment and cytometric analysis of DNA content

For double thymidine synchronization, 5-day (from single cell seeding) P9T organoid cultures were harvested (with Dispase), then reseeded in 8-well Nunc™ Lab-Tek II Chamber Slides, in CRC medium. After 3hr organoids were incubated with 2mM thymidine (Sigma-Aldrich) for 20hr, then released for 7hr by 3-times washing with CRC medium. Next, organoids were blocked again for 20hr with 2mM thymidine and then maintained in thymidine for another 24hr in the presence of vehicle (DMSO), 120nM VNRB, 3μM Lap+22nM Tram, or 120nM VNRB+3μM Lap+22nM Tram. Images were acquired on an EVOS imaging system (ThermoFisher).

For EdU incorporation studies, P9T organoid cultures were subjected to a double thymidine block (48hr in total), washed extensively (3 times 10 min) and then released in CRC medium containing 500 nM EdU (ThermoFisher) for 16hr. Parallel P9T cultures (not blocked with thymidine), incubated with EdU, were used as controls. Treated organoids were harvested with dispase, trypsinized and filtered to obtain single cells (as described before). Single cells were fixed in PBS/ethanol (30/70%) and then stained with a Alexa 488-EdU Click-iT reaction kit, according to the manufacturers' protocol (ThermoFisher). DNA was stained using 10 μg/mL Hoechst33342. Cells were analyzed on a BD FACSCelesta flow cytometer. Singlet gating and DNA quantification were performed using FlowJo (BD).

Western blot analysis

P9T PDOs were treated as indicated in the figure legends. The pan-Caspase inhibitor Z-VAD-FMK was used at 50μM and co-administered with VNRB in the triplet-combination where indicated. Prior to cell lysis, organoids were incubated with 1 mg/mL dispase II (Invitrogen) for 10 min at 37°C to digest the BME. Organoids were lysed using RIPA buffer (Cell Signaling Technology), complemented with 5mM NaF and Complete protease inhibitors (Roche). PDOX tissue samples were processed by snap-freezing in liquid N_2 and

grinded using ice-cold mortar and pestle. Lysates were prepared using hot SDS-buffer (1% SDS, 10mM EDTA, preheated to 95°C), containing 5mM NaF, 2mM $NaVO_3$ and protease inhibitors. Protein content was quantified using a BCA protein assay kit (PierceTM). Protein lysates were run on SDS-PAGE gels and transferred to PVDF membranes (Millipore). Membranes were blocked and probed with antibodies directed against ERK1/2 (RRID:AB_390779) phospho-ERK (RRID:AB_331646), BIM (RRID:AB_10692515), cleaved PARP (Asp214) (RRID:AB_10699459), Mcl-1 (D35A5, Cat#5453), BCL-xL (RRID:AB_2228008), cleaved Caspase-3 (Asp175) (RRID:AB_2341188), $pEGFR^{Y1068}$ (#2234), EGFR (#4267) from Cell Signaling Technology, Vinculin (RRID:AB_477629) and β-Actin (RRID:AB_476697) from Sigma-Aldrich.

PDO xenograft experiments and pharmacokinetic analysis in mice

For xenograft experiments P9T PDOs, grown for 3 days (seeded as single cells) were harvested using dispase, washed and then filtered using a 100μm cell strainer (VWR). Organoids were resuspended in CRC medium containing 50% MG and 10% collagen type I (BD Biosciences) and ~200000 organoids/100μL were injected (one-sided) subcutaneously into NOD-Scid mice. Mice with established tumors (with a volume of ≥150 mm^3, measured on the first weekday) were treated with a combination of Lapatinib (Lap), administered via oral gavage. Lap (25 mg/mL) was dissolved in DMSO and mixed 1 + 1 with Cremophor EL (CrEL). At the day of use, the DMSO:CrEL mixture was diluted 1 + 4 to achieve a final concentration of 2.5 mg/mL. Lapatinib was given twice daily, 12.5 mg/kg (5 μL per gram body weight) in the morning and 25 mg/kg (10 μL per gram body weight) in the afternoon with 8 h time difference). Trametinib (Tra) dissolved 1 mg/mL in DMSO was diluted 1:400 in 2.0% (w/v) β-hydroxy-cyclodextrin in 2.5 mM HCl. 20 mg/mL of sucrose was added and this was provided as drinking water containing 2.5 μg/mL of trametinib). Both compounds were administered in a 5 days on (drugs), 2 days off schedule. For the triplet-drug combination, Vinorelbine was administered on day 3 intravenously (10 mg/kg) in addition to the before mentioned Lap/Tra combination. One treatment cycle consisted of 2 weeks treatment and 1 week rest. Tumor volumes were evaluated three times per week by caliper and the approximate volume of the mass was calculated using the formula $D \cdot d^2/2$, where D is the major tumor axis and d is the minor tumor axis. Body weights were evaluated on a daily basis during treatment and 3 times per week during rest. Mice were sacrificed when the tumor volume reached 1500mm^3. If a tumor reached the maximum volume before the end of the treatment, a value of 1500mm^3 was assigned until the end of the protocol to calculate the mean tumor volume (for both treatment and control groups).

To determine the pharmacokinetics and tolerability of Lap/Tra combined treatment, 5 NSG mice were treated continuously (without a rest week) using a 5 days on/2 days off regimen, for a total of 38 days. Lap/Tra dosing and administration routes were similar as already described. On day 3 and 32 of treatment, blood samples were taken 1, 2, 4, 8 and 24hr after the first dose (25 mg/kg) of Lapatinib. Lap/Tra serum concentrations were evaluated using an LC-MS/MS method. Briefly, 5 μL of plasma samples were vortex-mixed with 30 μL of acetonitrile:formic acid (1000:1; v/v), containing 25 nM of trametinib-d6 and lapatinib-d3 and centrifuged 5 min (20,000 g, 4°C). A volume of 20 μL of the supernatant was diluted with 160 μL of water and 20 μl was injected on a Zorbax Extend C18 column (100 × 2 mm; ID) using a linear gradient from 20% to 95% methanol in 0.1% formic acid in water at a flow rate of 0.4 mL/min. MS detection using MRM mode using ion pairs 581.1/365.1 (lapatinib) 584.1/366.1 (lapatinib-d3), 616.2/254.2 (trametinib) and 622.2/260.2 (trametinib-d6).

Histology procedures and image analysis on PDOX tissues

Mice were sacrificed (2 mice for each treatment) on day 5 of treatment with the indicated drugs and dissected PDOX tissues were immediately processed for histology. PDOX tissues were fixed in 10% neutral buffered formalin and embedded in paraffin. Sections were subjected to H&E and Alcian blue staining as well as immunohistochemical (IHC) staining. The primary antibodies used for IHC staining: Cleaved Caspase-3 D3E9 (Cell Signaling Technology, RRID: AB_10897512), anti-human Cytokeratin Clone CAM5.2 (BD Biosciences, RRID: AB_2800363) and anti-human Ki-67 clone MONX10283 (Cell Sciences, RRID: AB_1833494). Cleaved Caspase3 stained images were analyzed using QuPath-0.3.2 (Bankhead, P. et al., Scientific Reports, 2017, QuPath: Open source software for digital pathology image analysis.). Cell nuclei (marked by Alcian blue) were automatically detected from manually annotated tumor epithelium and cleaved Caspase3 positive cells (marked by DAB) were quantified using an intensity-based threshold (DAB OD max parameter). The percentage of positive cells was determined from >10,000 detected cells per tissue section.

QUANTIFICATION AND STATISTICAL ANALYSIS

For each experiment, sample size, number of replicates and associated statistical data can be found in the result section and figure legends and/or the respective STAR Methods section. For comparison between more than two sample groups, ordinary one-way ANOVA was performed, using uncorrected Fisher's LSD for post-hoc analysis. For comparison between two sample groups, statistical analysis was conducted using the two-tailed unpaired Student's t-test. To establish the effects of drug treatment in mice over time, two-way RM-ANOVA (full-model) analysis was performed using Geisser-Greenhouse correction (for deviation of sphericity). Post-hoc analysis of individual time points was performed using uncorrected Fisher's LSD test. Pearson correlation analysis and statistical significance evaluated by the above-mentioned tests were all performed in Graphpad Prism (v9).